Thesis for the degree
Master of Science

Submitted to the Scientific Council of the
Weizmann Institute of Science
Rehovot, Israel

עבודת גמר (תזה) לתואר
מוסמך למדעים

מוגשת למועצה המדעית של
מכון ויצמן למדע
רחובות, ישראל

By
Dean Mark

מאת
דין מרק

תופעות מזוסקופיות של על-מוליכים טופולוגיים
Mesoscopic effects in topological superconductivity

Advisor:
Prof. Yuval Oreg

מנחה:
פרופ' יובל אורג

Aug. 2015

אלול תשע"ה

To my better half Yael
for everything and more

Contents

Acknowledgments **1**

Abstract **3**

1 Introduction **5**

2 Theoretical Background **11**

2.1 Majorana Fermions 11

2.1.1 Topological Majorana Fermions and Kitaev's Chain 12

2.1.2 Semiconducting Nanowire Setup 14

2.1.3 Experimental Signatures of Majorana Bound States 18

2.2 Landauer-Büttiker-Imry Formalism 20

2.2.1 Finite Temperature 22

2.3 Green's Function and the Scattering Matrix 23

2.3.1 Scattering Matrix and the Transmission function 23

2.3.2 Single-particle Green's function and the Scattering matrix . . 24

2.4 Tight Binding Model and Simulation (the method of finite differences) 28

2.4.1 Semiconducting Nanowire Hamiltonian 28

2.4.2 Aharonov-Bohm Ring Hamiltonian 30

2.4.3 Proximity Coupling to a SC 31

2.4.4 Modeling Experimental Systems 32

3 Analytic Calculations **35**

3.1 Temperature Dependence of the Conductance 36

3.2 Temperature Dependence of the Visibility 38

3.2.1 Visibility of a Breit-Wigner Resonance 39

3.2.2 Constant Visibility $\Gamma_1 = \Gamma_2$, $G_{0,1} \geq G_{0,2}$ 41

3.2.3 Increasing Visibility $\Gamma_1 > \Gamma_2$, $G_{0,1} \geq G_{0,2}$ 41

3.2.4 Decreasing and Non-Monotonic Visibility $\Gamma_1 > \Gamma_2$, $G_{0,1} < G_{0,2}$ 41

3.3 Simple Analytic Model 43
3.3.1 Conductance of a MBS 43
3.3.2 Visibility of a MBS 45
3.3.3 Conductance of a Zero Bias ABS 47
3.3.4 Visibility of a Zero Bias ABS 49
3.4 Conclusion 51

4 Numerical Calculations and Results 53
4.1 Tight Binding Simulation 55
4.2 Wire Configuration 57
4.3 Conclusion 64

5 Discussion 67

Bibliography 69

Nomenclature 73

Acknowledgments

First and foremost, I would like to thank my advisor Prof. Yuval Oreg for guiding me through this work, for taking time whenever I came up with questions and helping me move the Thesis forward, and mainly for the patience and support that was needed to see this work to completion.

I would also like to express my gratitude to Arbel Haim, for teaching me the practicalities of the subject, for countless fruitful discussions, and helping me turn raw ideas into reality.

Thanks to my parents, who taught me to aim high and gave me the confidence to do so. To my family and friends, for their support and acceptance of my absence while studying.

Most of all - thanks to my better half Yael, who gave me the strength and support I needed, and also the most wonderful present I could ask for - our son, Ido.

Abstract

Majorana fermions in condensed matter physics are emergent bound states at zero energy. These states are predicted to occur at topological defects in superconductors and their boundaries. Recent investigations suggest the existence of these states in semiconductor nanowires with proximity induced superconductivity and a Zeeman field. Although the experimentally observed zero bias tunneling peak and fractional ac-Josephson effect can be taken as necessary signatures of a Majorana bound state, there still exist alternative explanations to these observations. Thus, neither of them constitutes a sufficient "smoking gun" experiment. In this research we will present an experimental signature for the detection of Majorana bound states. We consider a normal lead with an Aharonov-Bohm ring, tunnel coupled to a Majorana bound state. We expect that decoherence effects will increase with temperature hence the visibility should decrease with temperature. In striking contrast, we find that the visibility for such a system with a Majorana bound state is a strictly increasing function of temperature, which tends to zero at zero temperature. This behavior is independent of the exact details of the coupling to the lead. In comparison we show that for a low energy Andreev bound state the visibility can assume increasing, decreasing, constant or non-monotonic behavior. We present an analytic proof for these claims. To corroborate the results, we performed a numerical simulation of an experimentally realizable system, and confirm that the visibility of a Majorana bound state is indeed an increasing function of the temperature.

1 Introduction

Majorana fermions are fermionic particles expected to be their own antiparticles [1]. Although elementary particles of the Majorana type have not been identified yet, quasi-particles with Majorana-like properties, born from interacting electrons in the solid, have been predicted to exist. These excitations are expected to have zero energy, meaning that they occur at the chemical potential. Specifically, the MFs will be zero energy modes localized on the boundaries of topological superconductors, and they will be called "Majorana bound states" (MBS) or alternatively "Majorana zero modes".

Let γ denote the operator corresponding to one of these Majorana bound states. This object is its own antiparticle in the sense that $\gamma = \gamma^\dagger$ and $\gamma^2 = 1$. Unlike an ordinary electronic state in a metal, there is no meaning to γ being occupied or unoccupied. Rather, γ should be viewed as a fractionalized zero mode comprising 'half' of a fermion. More precisely, a pair of Majorana bound states must be combined via $f = \gamma_1 + i\gamma_2$ to obtain a fermionic state with a well-defined occupation number. This operator represents a conventional fermion, but remains nontrivial in two respects. First, γ_1 and γ_2 may be localized arbitrarily far apart from one another; consequently f encodes a highly non-local entanglement, allowing the use of this state as a qubit which is resilient to decoherence. Second, one can empty or fill the non-local state described by f with no energy cost, resulting in a ground-state degeneracy. These two properties underpin by far the most interesting consequence of Majorana fermions - the emergence of non-Abelian statistics.

Non-Abelian statistic is different and more complex than conventional anyons. The adiabatic interchanging (braiding) of two Majorana bound states result not only in a change of the phase of the quantum mechanical wave-function, but also in the change of the internal states of the modes. Such braiding operations transform the system non-commutatively between its degenerate ground states.

A braiding operation of the form above is called topological, because it is fully

determined by the topology of the braiding path. This power to evolve simple operations in physical space into complex motions in an exponentially large Hilbert space is thought to provide qualitatively new and powerful methods for quantum information processing. Thus the search for the Majorana fermions is fueled by the potential for a major technological revolution in the field of quantum computation.

Majorana fermions have recently been proposed to exist in the topologically superconducting phase of a spin-orbit coupled semiconductor 2D thin film [2, 3], and a 1D nanowire [4, 5] with proximity induced s-wave superconductivity and Zeeman splitting from a sufficiently large magnetic field.

One simple detection scheme proposed for the Majorana bound states is to measure their unique tunneling signatures. The hallmark of the Majorana bound state is the appearance of a quantized zero bias conduction peak of $G = 2e^2/h$ when the system is in the topological phase [6, 7]. The quantized value is predicted at zero temperature, while for finite temperatures we expect thermal smearing of the peak. This peak is robust to any specific details of the system hosting the Majorana bound states, or to the details of the coupling between the probe and the Majorana bound state.

Following the proposal for the 1D semiconducting nanowire, a series of transport experiments realizing this setup were conducted [8, 9, 10]. The experiments reported the observation of a zero-bias conductance peak, with the peak emerging at a certain critical magnetic field. The zero bias peak was found to be robust to further increases in the magnetic field until a certain field in which it splits into two peaks. The peak was also found to be robust to changes in the angle of the applied magnetic field within certain boundaries. These findings are consistent with the presence of a Majorana bound state appearing when the system is in the topological phase and disappearing when the system returns to the topologically trivial state.

While these experiments are promising, several other mechanisms have been proposed in which a zero bias peak appears. Some alternatives are an accidental Andreev bound state at zero bias, the Kondo effect [11] and weak anti-localization [12]. It is therefore important to have a physical signature beyond the zero bias peak that can distinguish the Majorana bound state from the different scenarios.

In this Thesis, we present a robust signature for the detection of a Majorana bound state. We propose using a normal lead with an Aharonov-Bohm flux ring as a probe, and connect this lead to the Majorana bound state. Due to the Aharonov-Bohm ef-

fect the continuance through the ring oscillates with the application of flux through the ring. The visibility, v, of the setup is defined as the ratio between the amplitude of the oscillations and its mean value (See Eq. 3.16). In such a setup, we suggest to measure the visibility of the zero bias conductance peak as a function of temperature. For a Majorana bound state, the visibility is a strictly increasing function of temperature, with zero visibility at zero temperature. In contrast, we show that for an Andreev bound state the visibility can assume increasing, decreasing, constant or non-monotonic behavior. Thus by measuring the visibility of a conductance peak as a function of temperature we can rule out the case of a Majorana bound state if the visibility is not strictly increasing. This property is robust and does not depend on the coupling constant or any other details of the model. These results will be proven analytically and exemplified in this Thesis.

The analytic proof uses the fact that while the zero temperature conductance height of the Majorana peak is robust, the width of the peak depends on the coupling to the probe. By varying the flux through the Aharonov-Bohm ring, we change the coupling strength to the Majorana bound state and change the width of the peak. These two facts imply the suggested behavior. In a sense, the visibility at finite temperature allows us to gain some knowledge as to the nature of the zero temperature conductance.

To strengthen the analytic results, we performed a numerical simulation of an experimentally realizable system, and find that the visibility indeed acts as expected. We consider a system used in recent experiments which consists of a 1D nanowire with Rashba spin-orbit coupling and a Zeeman field, proximity coupled to an s-wave superconductor (Fig. 1.1). First we tune the system so that it hosts a low energy Andreev bound state and calculate the visibility as a function of temperature (Fig. 1.2a). The visibility of the Andreev bound state is a decreasing function of temperature. We then tune the system to the topological phase performing the same calculation (Fig. 1.2b), here we also fit the results with the theoretical prediction for an ideal MBS. We see that the visibility of the Majorana bound state from the numerical results agree with the analytic results.

The main text of the Thesis is divided into three main chapters. In Chapter 2 we give a detailed description of the theoretical background and tools used in the Thesis. We first give an overview on the subject of Majorana fermions in solid state systems in Section 2.1. We present the Kitaev chain model followed by the practi-

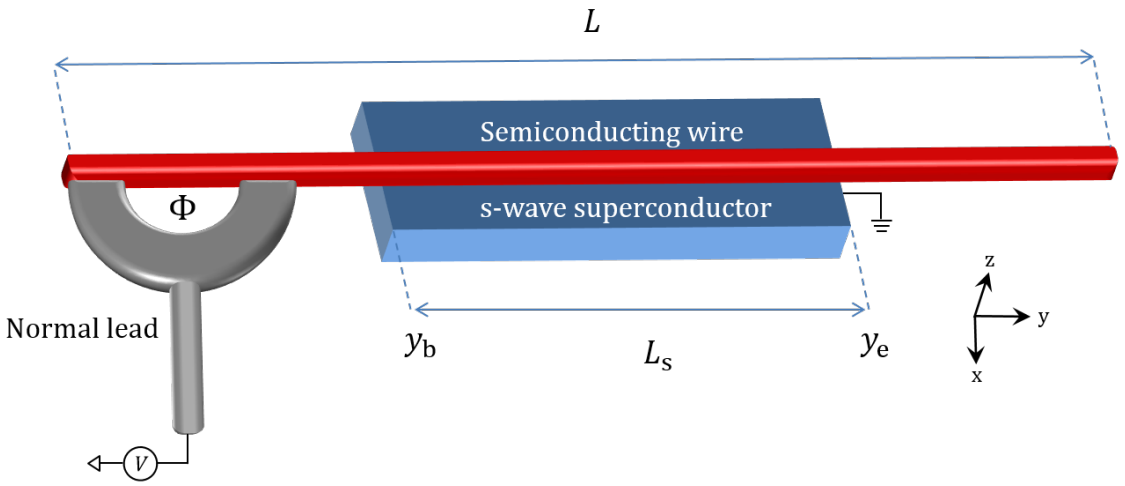

Figure 1.1: Experimental setup. A semiconducting 1D nanowire proximity coupled to an s-wave superconducting lead. A normal lead is connected to the left. The normal lead and part of the wire form an Aharonov-Bohm flux ring. The parameters are taken in accordance to a recent experiment [8]. We take the spin orbit energy to be $E_{so} = 50\,\mu$eV, the induced superconducting gap to be $\Delta_0 = 250\,\mu$eV, and the spin orbit length to be $l_{so} = 200\,$nm. The length of the wire is taken to be $L = 2500\,$nm, with $L_s = 1385\,$nm.

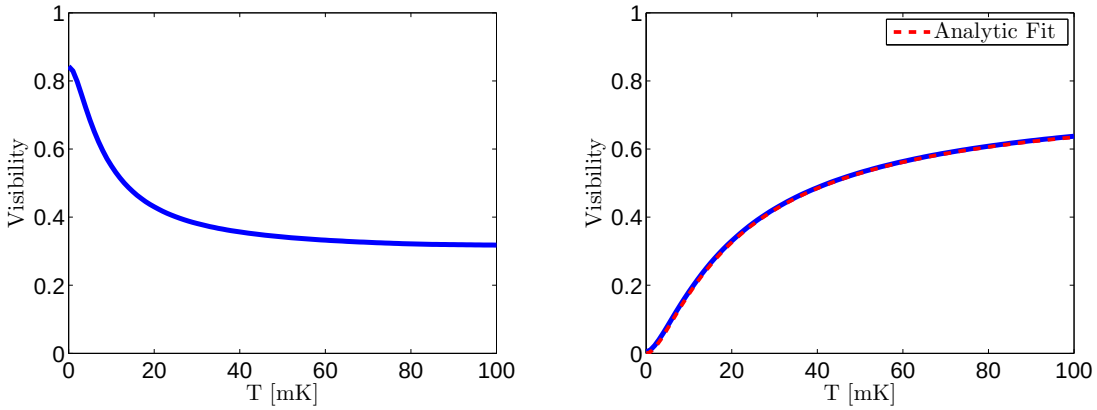

(a) Andreev Bound State **(b)** Majorana Bound State

Figure 1.2: Visibility as a function of temperature. (a) Visibility of the Andreev bound state. Monotonically decreasing function of temperature. (b) Visibility of the Majorana bound state with an analytic fit. For details of the the simulation see main text (Section 4.2). This closely resembles the topological state with a monotonically increasing function of temperature which tends to zero at zero temperature. There is a good fit with the analytic expressions of visibility for an ideal Majorana bound state.

cal realization of Kitaev's model with a 1D semiconducting nanowire. We review several tunneling signatures for verifying the existence of Majorana fermions in an experimental system together with recent experiments. In Section 2.2 we describe the Landauer-Büttiker-Imry Formalism which is used to calculate the finite temperature conductance of a coherent conductor in terms of the transmission probabilities through the system. In Section 2.3 we review the relation between the Green's function and the scattering matrix (S-Matrix). By computing the Green's function of a system it is possible to calculate the S-Matrix. The transmission probabilities then correspond to elements of the S-Matrix. Hence, once the Green's function of a system is calculated the conductance through the system is known. In order to calculate the Green's function of continuum systems, we discretize the continuum. The technical details of this method are explained in Section 2.4.

Chapters 3 and 4 mark the second part where we present our results. Chapter 3 presents the analytic results of the Thesis. Here we prove our main result that the visibility of a Majorana bound state is a strictly increasing function of temperature, which tends to zero at zero temperature. We also show that the visibility of a low energy Andreev bound state can assume increasing, decreasing, constant or non-monotonic behavior. This is done by writing an analytic expression for the visibility of a general Breit-Wigner resonance, and examining how the parameters of the zero temperature conductance determine the behavior of the visibility at any temperature, producing the different monotonic and non-monotonic behaviors. Two simple analytic models are then presented, one for a system hosting a Majorana bound state and another hosting an Andreev bound state. We calculate the conductance of these models and show that the Majorana bound state falls under the category in which the visibility is strictly increasing. For the Andreev bound state we show the different behaviors by selecting different parameters of the model.

We conclude the Thesis with Chapter 4. In this chapter we will present numerical simulations of a system consisting of a 1D semiconducting nanowire hosting Majorana bound states. The wire is connected to a normal lead with an attached Aharonov-Bohm flux ring. We will show that the wire can host a Majorana bound state and an Andreev bound state which exhibit a zero bias conductance peak. We will be able to distinguish between them by looking at the visibility as a function of temperature, thus corroborating the analytic results.

2 Theoretical Background

2.1 Majorana Fermions

In 1928 Dirac introduced his equation that describes quantum relativistic spin 1/2 particles. The solutions of this equation are in general complex, and the equation supports the description of electrons and an anti-electron partner – the positron. Ten years later, Ettore Majorana showed that Dirac's equation also supports real solutions, the so called Majorana fermions which are their own antiparticles. The search for Majorana fermion particles has not been concluded, and it is not yet known whether a Majorana particle exists in nature.

In condensed matter physics the term "Majorana fermion" (MF) has been borrowed to describe an object that carries half of the properties of an electronic degree of freedom. Given an electron creation operator $c^\dagger$, one can formally decompose the operator into its real and imaginary part

$$c^\dagger = \frac{\gamma_1 + i\gamma_2}{2}, \tag{2.1}$$

$$\gamma_\alpha = \gamma_\alpha^\dagger, \tag{2.2}$$

$$\{\gamma_\alpha, \gamma_\beta\} = 2\delta_{\alpha\beta}, \tag{2.3}$$

where the γ operators are MF operators, in the sense that they are their own 'anti-particles'.

Contrary to the high energy MF, the condensed matter MF does not describe particles that behave according to Dirac's equation. As we have seen above, condensed matter MFs are obtained by a symmetric linear combination of creation and annihilation operators of the same fermion. One may be under the impression that they define a new fermionic particle, but this is not true since no vacuum state can be defined for these operators. Furthermore, it is not possible to measure the occupation

number of the MFs, as their number operator $\gamma^\dagger\gamma = \gamma^2 = 1$ is a c-number.

Hence, MFs in our context are not elementary particles but are nontrivial emergent excitations. In the systems we will present in the following sections, MF states will be defined relative to the superconducting ground state. Specifically, the MFs will be zero energy modes localized on the boundaries of topological superconductors, and they will be called "Majorana bound states" (MBS) or alternatively "Majorana zero modes".

These MBSs must always be paired to form a normal fermionic state with a well defined occupation number. While the combined fermion obeys the usual anti-commutation relations, it has two interesting properties. First, γ_1 and γ_2 may localize far apart from each other resulting in a highly non-local entanglement. Second, the combined fermion has zero energy, resulting in a ground state degeneracy.

In the next chapter we will present a simple example of a topological superconductor which hosts MBSs.

2.1.1 Topological Majorana Fermions and Kitaev's Chain

This section introduces a toy model for a topological 1D spinless p-wave superconductor that supports Majorana fermions. This model is named the "Kitaev Chain", and was introduced by A. Kitaev [13] in 2001. In this model the MBSs appear in a simple and intuitive fashion. The Kitaev lattice Hamiltonian reads

$$H = -\mu \sum_{i=1}^{N} c_i^\dagger c_i - \frac{1}{2} \sum_{i=1}^{N-1} \left(t c_i^\dagger c_{i+1} + \Delta c_i c_{i+1} + \text{h.c.} \right), \tag{2.4}$$

where the $c_i^\dagger$ operators are creation operators for a fermion on site i of the chain, μ is the chemical potential, $t \geq 0$ is the nearest neighbor hopping strength, Δ is the superconducting pairing term and we have chosen $\Delta = \Delta^*$. This Hamiltonian can be rewritten in the MF basis by decomposing each spinless fermion into two MFs which obey the canonical MF relations

$$c_i = \gamma_{1,i} + i\gamma_{2,i}, \tag{2.5}$$

$$\gamma_{\alpha,i} = \gamma_{\alpha,i}^\dagger, \tag{2.6}$$

$$\{\gamma_{\alpha,i}, \gamma_{\beta,j}\} = 2\delta_{\alpha\beta}\delta_{ij}. \tag{2.7}$$

In this basis H becomes

$$\begin{aligned} H &= -\frac{\mu}{2}\sum_{i=1}^{N}\left(1+i\gamma_{1,i}\gamma_{2,i}\right) \\ &\quad -\frac{i}{4}\sum_{i=1}^{N-1}\left[\left(\Delta+t\right)\gamma_{1,i}\gamma_{2,i+1}+\left(\Delta-t\right)\gamma_{2,i}\gamma_{1,i+1}\right]. \end{aligned} \tag{2.8}$$

Let us choose $\mu = 0$ and $\Delta = t \neq 0$, the Hamiltonian becomes

$$H = -i\frac{t}{2}\sum_{i=1}^{N-1}\gamma_{1,i}\gamma_{2,i+1}. \tag{2.9}$$

One could now define a new set of fermionic operators $d_i^\dagger$,d_i which couple MFs from adjacent sites, and a non local operator a, and diagonalize the Hamiltonian. The result is

$$H = t\sum_{i=1}^{N-1}\left(d_i^\dagger d_i-\frac{1}{2}\right)+0\cdot a^\dagger a, \tag{2.10}$$

with $d_i = \frac{1}{2}\left(\gamma_{2,i+1}+i\gamma_{1,i}\right)$ and $a = \frac{1}{2}\left(\gamma_{2,1}+i\gamma_{1,N}\right)$.

Notice that the ground state is doubly degenerate, as the states with $n_a = \left\langle a^\dagger a\right\rangle = 0$ or 1 have the same energy. The two states have different parity. Assuming N is odd, the vacuum $|0\rangle$ has even parity and includes an even number of a-fermions. The second ground state $|1\rangle$ contains one a-fermion and has odd parity. This differs from a conventional gapped superconductor, in which the ground state always has even parity, so all electrons can form Cooper pairs.

The fermionic state a is quite interesting. It is a zero energy state that is a coherent superposition of two MFs coming from the two edges of the 1D wire, at $i = 1$ and $i = N$. Thus the a state forms a highly non-local fermion.

The appearance of localized zero-energy Majorana end-states and the ground state degeneracy arise from the topological nature of the chain. The parameters chosen above insert the wire in a topological phase, while the vacuum that borders the wire is trivial. These two phases cannot be smoothly connected, hence the gap must close at the wire boundaries.

Because the origin of the Majorana edge states is topological, their existence does not rely on a particular fine tuned limit as shown above. Although, in a more

general parameter choice with $\mu \neq 0$ and $t \neq \Delta$ while still in the topological phase, the MBSs that compose the a-fermion no longer consist solely of $\gamma_{2,1}$, $\gamma_{1,N}$. The a-fermion wavefunction now decays exponentially from both sides into the bulk of the wire.

The overlap of the wavefunction now results in a lifting of the degeneracy of the ground state, with finite splitting energy $E_{\mathrm{M}} \neq 0$. The $|0\rangle$ and $|1\rangle$ states now split into two states with splitting energies that scale as $E_{\mathrm{M}} \sim \mathrm{e}^{-L/\xi}$, where L is the length of the wire and ξ is the coherence length. Usually it is assumed that $L \gg \xi$ and this splitting can be neglected ($E_{\mathrm{M}} = 0$). However, in the numerical simulations we will later present, the energy splitting will be clearly present and will be directly addressed.

This ever present splitting that appears in finite systems means that in an experiment we cannot truly create the ideal a-fermion state. Nevertheless, looking at the correct parameters we will be able to create and measure states that closely resemble it.

2.1.2 Semiconducting Nanowire Setup

There are two main problems in the practical realization of Kitaev's chain: the presence of a p-wave superconductor, and that a long range superconducting order is assumed in a 1D system. In 2010 two similar works [4, 5] demonstrated how to create a system that obeys the Kitaev Hamiltonian using ingredients that are available in the lab: a quasi 1D semiconducting nanowire with strong spin-orbit coupling, a s-wave superconductor tunnel coupled to the wire, and a strong magnetic field.

The proximity of the wire to the superconductor turns the wire itself into a superconductor via the proximity effect. This effect allows the wire to inherit long range order cooper pairing from the superconductor. The magnetic field creates time reversal symmetry breaking. These two effects together with spin-orbit coupling converts the 1D system into a p-wave superconductor, with an effectively long range order due to the absence of phase fluctuations in the bulk 3D superconductor.

To see this in more detail, we start with a general Hamiltonian [5] for a 1D wire lying along the y axis, with spin orbit interaction u along the z axis, and a magnetic field B along the x axis (Fig. 2.1). The wire is in contact with a superconductor,

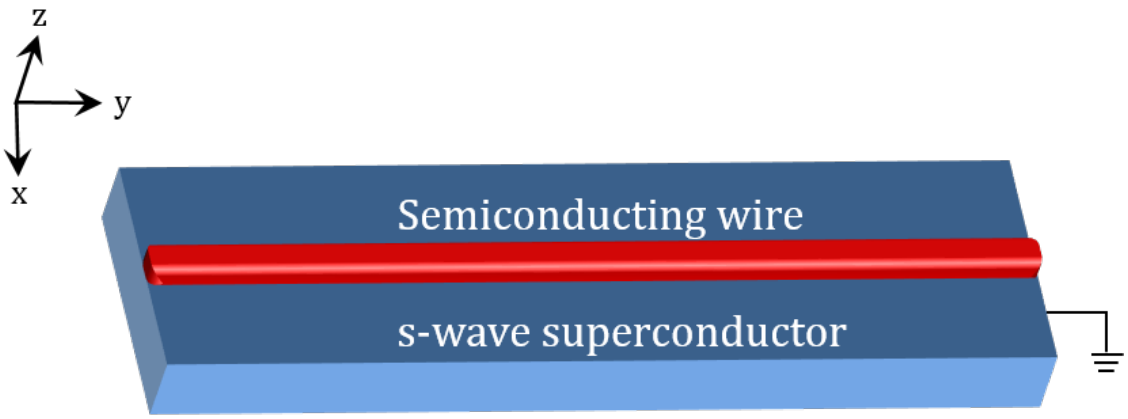

Figure 2.1: The setup of the nanowire based proposal

with proximity strength Δ. The Hamiltonian of the system is

$$
\begin{aligned}
H &= \int \Psi^{\dagger}(y)\,\mathcal{H}\Psi(y)\,dy, && (2.11)\\
\mathcal{H} &= \left[\hat{p}^2/2m-\mu(y)\right]\tau_z+\alpha\hat{p}\sigma_z\tau_z+B(y)\,\sigma_x+\Delta(y)\,\tau_x, && (2.12)\\
\Psi^{\dagger} &= \left(\psi_{\uparrow}^{\dagger},\psi_{\downarrow}^{\dagger},\psi_{\downarrow},-\psi_{\uparrow}\right), && (2.13)
\end{aligned}
$$

where $\psi_{\uparrow,(\downarrow)}(y)$ annihilates spin up (down) electrons at position y, α gives the Rashba spin-orbit coupling, B gives the Zeeman energy, Δ the induced superconductivity and μ the chemical potential. The Pauli matrices σ, τ operate in the spin and particle-hole space, respectively.

To better understand the system, we write the Hamiltonian in k space

$$
\begin{aligned}
H &= \sum_k \Psi_k^{\dagger}\mathcal{H}(k)\,\Psi_k, && (2.14)\\
\mathcal{H}(k) &= \left[p^2/2m-\mu\right]\tau_z-\alpha p\sigma_z\tau_z+B\sigma_x+\Delta\tau_x, && (2.15)\\
\Psi_k^{\dagger} &= \left(\psi_{k,\uparrow}^{\dagger},\psi_{k,\downarrow}^{\dagger},\psi_{-k,\downarrow},-\psi_{-k,\uparrow}\right). && (2.16)
\end{aligned}
$$

We then solve the system with $\Delta=0$. The Hamiltonian is easily diagonalized with electron eigenvalues and eigenvectors

$$
\begin{aligned}
E_{\pm} &= p^2/2m-\mu\pm\sqrt{B^2+\alpha^2p^2}, && (2.17)\\
\psi_{\pm}^{\dagger} &\sim \left(\,-\alpha p\pm\sqrt{B^2+\alpha^2p^2},\quad B,\quad 0,\quad 0\,\right). && (2.18)
\end{aligned}
$$

The spin orbit coupling α splits the two degenerate spin bands into two distinct parabolas, while the Zeeman energy B opens a gap between the two bands, removing the degeneracy at $p = 0$. Additionally, in the limit of large Zeeman energy $|B| \gg E_{\mathrm{SO}}$ where $E_{\mathrm{SO}} = \frac{m\alpha^2}{2}$, the electrons in a single band polarize and have the same p-independent polarization. Therefore, if the chemical potential is set such that the Fermi surface is inside the $p = 0$ gap, then the low energy effective Hamiltonian is essentially spinless. In this limit, we indicate the lower band species as ψ_-, and the upper band species as ψ_+.

We now include the effect of the superconducting s-wave pairing $\Delta > 0$ which is induced by the proximity effect. The expressions for the zero momentum gap and the Fermi momentum gap are

$$E_{\mathrm{g},p=0} = 2\left|B - \sqrt{\Delta^2 + \mu^2}\right|, \tag{2.19}$$

$$E_{\mathrm{g},p_{\mathrm{F}}} = 2\sqrt{\frac{\Delta^2 m\alpha^2}{B}}. \tag{2.20}$$

Here we assume a constant Zeeman energy $B > 0$, and that the chemical potential is placed in the spinless regime mentioned above $|B| > |\mu|$. For small Δ the gap at $p = p_{\mathrm{F}}$ opens and the superconductor enters the topological phase with MBSs appearing. With increasing Δ, the gap at $p = 0$ gradually closes. At $|B| = \sqrt{\Delta^2 + \mu^2}$ the gap completely closes, and for larger values of Δ the gap reopens with the superconductor now in the trivial phase. The criteria for topological superconductivity is thus

$$|B| > \sqrt{\Delta^2 + \mu^2}. \tag{2.21}$$

We will now show how the above Hamiltonian maps to the Kitaev chain model in the topological superconductor phase [14]. For simplicity, we consider the large Zeeman energy limit $|B| \gg E_{\mathrm{SO}}$, where the bands are approximately spinless

$$H_{\mathrm{prox}} = \sum_k \Delta\left[\psi^\dagger_{k,\uparrow}\psi^\dagger_{-k,\downarrow} - \psi^\dagger_{k,\downarrow}\psi^\dagger_{-k,\uparrow} + \mathrm{h.c.}\right]. \tag{2.22}$$

We express this Hamiltonian in terms of the new fields $\psi_\pm$ defined in Eq. 2.18 and

find

$$H_{\text{prox}} = -\sum_k \left[\Delta_p \left(\psi^\dagger_{k,+}\psi^\dagger_{-k,+} + \psi^\dagger_{k,-}\psi^\dagger_{-k,-}\right) + \Delta_s \psi^\dagger_{k,+}\psi^\dagger_{-k,-} + \text{h.c.}\right], \quad (2.23)$$

with

$$\Delta_p = \frac{\alpha p \Delta}{\sqrt{\alpha^2 p^2 + B^2}}, \quad \Delta_s = \frac{2B\Delta}{\sqrt{\alpha^2 p^2 + B^2}} \ . \quad (2.24)$$

Therefore a p-wave intra-band pairing appears in the Hamiltonian. This analysis provides a clear route towards a realization of the Kitaev model. In the spinless limit, the band gap is large, this allows us to consider a single-band model and ignore the higher band. Using this assumption one obtains the effective low band Hamiltonian which is equivalent to the Kitaev Hamiltonian (Eq. 2.4)

$$\begin{aligned} H &= \sum_k \Psi^\dagger_{k,-}\left[p^2/2m - \mu - |B|\right]\Psi_{k,-} \\ &\quad -\Delta_{\text{eff}}\left[\psi^\dagger_{k,-}\psi^\dagger_{-k,-} + \text{h.c.}\right], \quad (2.25) \\ \Delta_{\text{eff}} &= \frac{\alpha p \Delta}{\sqrt{\alpha^2 p^2 + B^2}}. \quad (2.26) \end{aligned}$$

We should note that as the Zeeman energy grows larger $B \gg \sqrt{\Delta^2 + \mu^2}$ the gap E_{g,p_F} gradually closes, and the cross band s-wave superconducting term Δ_s cannot be ignored anymore. This initially causes a significant overlap of the MFs, increasing the splitting energy E_M, and eventually closes the superconducting gap.

Although this setup successfully realizes the Kitaev chain, there are a few caveats related to it. First, the model assumes the simultaneous presence of superconductivity and a high magnetic field. Moreover, it is crucial to tune the chemical potential to the middle of the gap. This demands a large Zeeman energy to induce a large gap on the one hand, but on the other hand should not destroy the superconductivity. This can be achieved by using a material with large g-factor. Finally, it is important to have a large spin orbit coupling, since the gap at finite momentum is suppressed by the magnetic field (Eq. 2.26). Suitable candidate materials are InAs and InSb which have large g-factors and strong spin-orbit coupling.

2.1.3 Experimental Signatures of Majorana Bound States

Verifying the existence of Majorana fermions in condensed matter systems is an important topic in recent years, with many theoretical proposals which present different possible experimental signatures of MBSs. Following the scheme presented in the last section for a practical realization of the Kitaev chain, several experiments have also been conducted to experimentally realize the MBSs and measure them.

In this section we will focus on the tunneling signatures of the MBSs, both in theory and in experiments. We will see that although the experimental signatures that have been measured are promising, there are certain alternative theories that could explain the observations. Thus further signatures are needed to convincingly argue the case of the MBS, specifically ones which are easily measurable in the lab. Finding such signatures has been the aim of this research work, where we have identified a unique signature that is measurable in the lab (Chapter 3).

We start with the tunneling signature of the MBS [6, 7]. Assuming a wire configuration as presented in Subsection 2.1.2, we tunnel couple a single normal lead to the edge of the wire. At zero bias, when the system is in the trivial phase and the system possesses no subgap states, the zero temperature conductance from the lead to the superconductor is zero $G\left(E=0\right)=0$.

In the topological phase the conductance behaves differently. In the case of an infinite wire, the two MFs are infinitely separated with zero wavefunction overlap and splitting energy $E_{\mathrm{M}}=0$. In this case the MF induces a resonant Andreev reflection from the lead to the grounded superconductor. This means that an incident electron from the lead is converted into a backscattered hole with probability of unity, independent of the coupling strength, resulting in $G\left(E=0\right)=2\frac{e^2}{h}$ (Fig. 2.2a). The width of the conductance peak however, does depend on the coupling strength. In the case of a finite wire, the two MFs wavefunctions can overlap and a finite splitting arises $E_{\mathrm{M}}>0$. In this case the conductance peak splits into two. The zero bias conductance is close to zero $G\left(E=0\right)\sim 0$. At the splitting energy we have a maximum of the conductance, which in our model is close to $2\frac{e^2}{h}$, but in general $G\left(E=\pm E_{\mathrm{M}}\right)\leq 2\frac{e^2}{h}$ (Fig. 2.2b).

The resonant Andreev reflection through a MBS is different from the the usual Andreev reflection through an Andreev bound state (ABS), in which the conductance depends on the strength of the coupling. In Section 3.3 we will present an analytic

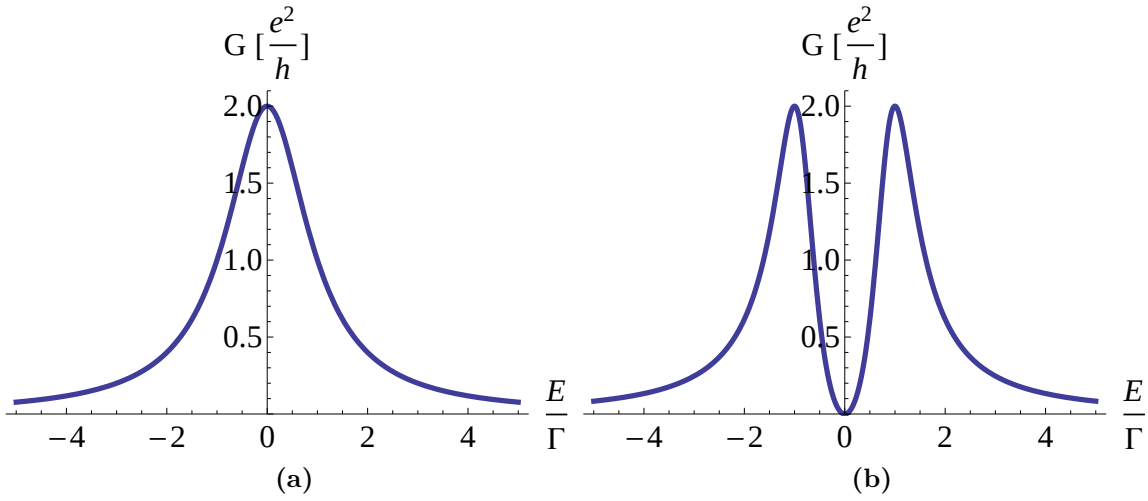

Figure 2.2: Zero temperature conductance through a single MBS in units of $\frac{e^2}{h}$ as a function of bias in units of width Γ. (a) Infinite wire configuration with zero MBS overlap and zero energy splitting $E_M = 0$. The conductance peak is a Lorentzian of height $2\frac{e^2}{h}$ and width Γ (b) Finite wire with MBS wavefunction overlap and splitting energy $E_M = \Gamma$. The zero energy conductance is close to zero, while the conductance at the splitting energy is close to $2\frac{e^2}{h}$ in our model.

model of the conductance through a MBS and an Andreev bound state and see a concrete example of this.

We now turn our attention to recent experiments in the field, aimed at experimentally measuring the MF. As mentioned earlier, following the proposal of the semiconducting nanowire setup described in the previous section, a series of transport experiments realizing this setup were conducted [8, 9, 10]. These experiments reported the observation of a zero-bias conductance peak (ZBCP) (Fig. 2.3). With the ZBCP emerging at a certain critical magnetic field. The ZBCP is robust to further increases in the magnetic field until a certain field in which it splits into two peaks. The observation is consistent with the presence of a MBS at finite temperature, see for example the results our numerical simulation in Fig. 4.2.

While these experiments are promising, several other mechanisms have been proposed in which a ZBCP appears. Some alternatives are an accidental Andreev bound state at zero bias, the Kondo effect [11] and weak anti-localization [12]. It is therefore important to have a physical signature beyond the ZBCP that can distinguish the MBS from the different scenarios.

In this Thesis, we will present the signature of the MBS in the visibility of the

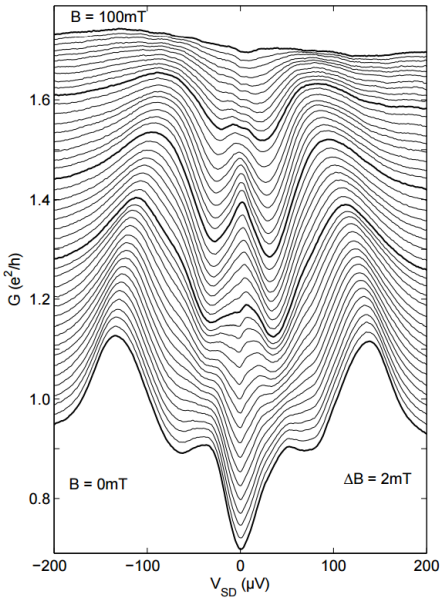

Figure 2.3: Conductance G versus bias potential V_{SD}. The estimated electron temperature in the wire was $T = 30\,\mathrm{mK}$. The measurement was performed for different values of the magnetic field from $0\,\mathrm{mT}$ to $100\,\mathrm{mT}$ in steps of $2\,\mathrm{mT}$. At $B \sim 30\,\mathrm{mT}$ a zero bias peak appears, and remains robust until $B \sim 70\,\mathrm{mT}$. Figure adapted from [10].

ZBCP as a function of temperature. In Chapter 3 we will show that the visibility of a MBS is strictly increasing, with zero visibility at zero temperature, while an ABS can assume many different behaviors.

2.2 Landauer-Büttiker-Imry Formalism

One of the most important measurements that characterizes a conducting material is it's conductance G. Since we are interested in coherent conductors, the framework used to describe the transport through these systems is called the Landauer-Büttiker-Imry Formalism. In this section we will describe the formalism, and see how the conductance can be described in terms of the transmission probabilities through the system. A detailed review of the the subject can be found in Ref. [15].

The standard setup for the theory (Fig. 2.4) assumes two contacts with an infinite number of conducting modes, connected to a conductor that has only a few conducting modes. The contacts are assumed to be reflectionless, this means that electrons enter from the conductor to the contacts with no reflection. The leads themselves

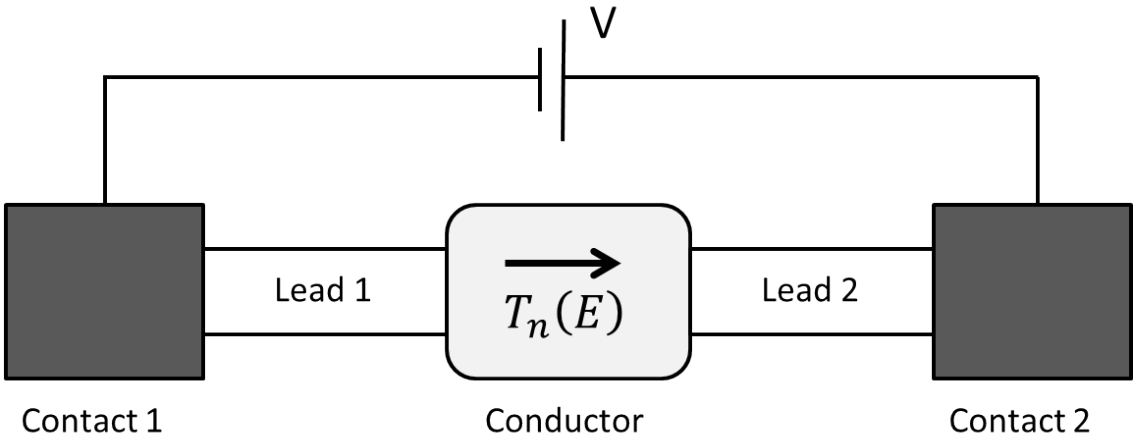

Figure 2.4: Typical setup for measuring the conductance G of a mesoscopic device. Two contacts with bias ΔV are connected to a conductor via leads. $T_n(E)$ denotes the transmission coefficient through the conductor for electrons in channel n at energy E.

are assumed to be ideal, without scattering.

We start with the case of a 2 probe device at zero temperature and low voltages. The conductance can be expressed in terms of the single electron transmission probabilities T_n, where T_n is the probability of an electron in mode n to transmit through the conductor. The result is known as the Landauer formula, in the spin independent case it is reduced to

$$G = \frac{2e^2}{h}\sum_n T_n\left(E_\mathrm{F}\right), \tag{2.27}$$

where the prefactor 2 in Eq. 2.27 accounts for the spin degrees of freedom, and the transmission probabilities are calculated at the Fermi energy. To explicitly account for the spins, in the event that the two spin channels have different transmission probabilities, we will sum them as different channels

$$G = \frac{e^2}{h}\sum_{n,\sigma} T_{n,\sigma}\left(E_\mathrm{F}\right), \tag{2.28}$$

where $\sigma \in \{\uparrow, \downarrow\}$.

The extension of this formula to the multi-terminal case is straightforward

$$G_{pq} = \frac{e^2}{h}\bar{T}_{p\leftarrow q}\left(E_{\mathrm{F}}\right), \tag{2.29}$$

$$\bar{T}_{p\leftarrow q}\left(E_{\mathrm{F}}\right) = \sum_{m\in p}\sum_{n\in q} T_{m\leftarrow n}\left(E_{\mathrm{F}}\right), \tag{2.30}$$

where the transmission probability $T_{m\leftarrow n}$ is equal to the probability of an electron to transmit from mode n in lead p to mode m in lead q. $\bar{T}_{p\leftarrow q}$ represents the total transmission from terminal q to terminal p. Here the spins are considered to be different modes of each lead.

2.2.1 Finite Temperature

Our expression for the Landauer-Büttiker-Imry formula (Eq. 2.29) was simplified by the assumption of zero temperature. At zero temperature the current is carried by a single channel around the Fermi energy. In general, transport takes place through multiple channels in the range

$$\mu_1 + k_B T > E > \mu_2 - k_B T, \tag{2.31}$$

where each channel can have a different transmission $\bar{T}$.

Assuming linear response, and assuming that the transmission function $\bar{T}$ is approximately constant over the energy range where transport occurs, we can write

$$I = G\left(E,T\right)\frac{\mu_1 - \mu_2}{e}, \tag{2.32}$$

where the conductance is given by

$$G\left(E,T\right) = \frac{e^2}{h}\int \bar{T}\left(E\right)\left(-\frac{\partial f_0}{\partial \epsilon}\right)_{\epsilon = E - E_{\mathrm{F}}} dE, \tag{2.33}$$

$$\frac{\partial f_0}{\partial \epsilon} = -\frac{d}{d\epsilon}\left(\frac{1}{\exp\left(\epsilon/k_B T\right)+1}\right) = \frac{1}{4k_B T}\mathrm{sech}^2\left(\frac{\epsilon}{2k_B T}\right). \tag{2.34}$$

We can also formally rewrite this formula in a form that will be useful later

$$G(E,T) = \int G(E+E_{\mathrm{F}},T=0)\left(-\frac{\partial f_0}{\partial E}\right)dE, \tag{2.35}$$

$$G(E,T=0) = \frac{e^2}{h}\bar{T}(E). \tag{2.36}$$

Next chapter we will see how to compute the transmission probabilities of a general conductor using the Green's functions formalism.

2.3 Green's Function and the Scattering Matrix

The Green's function is a mathematical tool used to solve differential equations [15]. This method is widely used in physics in general and specifically in condensed matter physics. In this chapter we will use this tool in order to calculate the transmission coefficients through a coherent conductor. The Green's function of a conductor gives us the response at any point of the conductor due to an excitation at any other point.

We start with a definition of the scattering matrix, and show how the transmission function can be expressed with elements of the S-matrix. We then define the Green's function, and show how it is related to the scattering matrix.

2.3.1 Scattering Matrix and the Transmission function

In Section 2.2 we have seen how the current can be expressed in terms of the transmission function (Eq. 2.27). In this section we will define the S-matrix, and show the relationship between it and the transmission function for coherent conductors. A coherent conductor is defined here as a conductor who's size is smaller than the phase relaxation length.

The S-matrix relates the outgoing current amplitudes to the incoming current amplitudes at the different leads. As an example, if there are two leads, each one with one propagating mode, we can write the S-matrix as follows

$$\begin{pmatrix} b_1 \\ b_2 \end{pmatrix} = \begin{bmatrix} s_{11} & s_{12} \\ s_{21} & s_{22} \end{bmatrix} \begin{pmatrix} a_1 \\ a_2 \end{pmatrix}, \tag{2.37}$$

where the outgoing current amplitudes are denoted by b, and the incoming current amplitudes are denoted by a. Generally, if there are M_{T} number of propagating modes in all the leads, then the scattering matrix will be of size $M_{\mathrm{T}} \times M_{\mathrm{T}}$. The scattering matrix can be calculated for specific structures through the use of the Green's function. In the next section we will see how the two are related.

The transmission probability T_{nm} is obtained by taking the squared magnitude of the corresponding S-matrix element

$$T_{m\leftarrow n} = |s_{m\leftarrow n}|^2 . \tag{2.38}$$

In the multi-terminal multi-channel case we are interested in the transmission function $\bar{T}_{pq}$ (Eq. 2.29). This quantity is obtained by use of Eq. 2.30.

One important property of the S-matrix is that it must be unitary. This is a direct consequence of the definition of the S-matrix as connecting current amplitudes between modes, combined with current conservation. This can be written in terms of the S-matrix itself

$$S^\dagger S = I = SS^\dagger, \tag{2.39}$$

and in terms of the S-matrix elements

$$\sum_{m=1}^{M_T} |s_{mn}|^2 = 1 = \sum_{n=1}^{M_T} |s_{mn}|^2 . \tag{2.40}$$

2.3.2 Single-particle Green's function and the Scattering matrix

In quantum mechanics, one is interested in solving the time-independent Schrödinger equation

$$[E - H]\,\psi\,(r) = 0, \tag{2.41}$$

where H is the Hamiltonian describing the system. We define the Green's function as the response of the system to a point like excitation as defined by the following

differential equation

$$[E - H]\, G(\mathbf{r}, \mathbf{r}', E) = \delta(\mathbf{r} - \mathbf{r}'), \tag{2.42}$$

$$[E - H]\, G(E) = I. \tag{2.43}$$

If E is not an eigenvalue of H, then the formal solution for this equation is given by

$$G(E) = [E - H]^{-1}, \tag{2.44}$$

$$G(\mathbf{r}, \mathbf{r}', E) = \langle \mathbf{r} |\, G(E)\, | \mathbf{r}' \rangle. \tag{2.45}$$

However, the inverse of a differential operator is not uniquely specified until we specify the boundary conditions. As a simple example, we consider a one-dimensional wire with a constant potential. Solving Eq. 2.42 gives rise to two solutions. One solution gives rise to outgoing waves originating at $\mathbf{r} = \mathbf{r}'$, this solution is referred to as the retarded Green's function (G^{R}). The other solution gives rise to incoming waves that originate in infinity and disappear at the point of excitation, this solution is referred to as the advanced Green's function (G^{A}). Both these solutions satisfy the same equation, but they correspond to different boundary conditions.

One common way to include the boundary conditions inside the equation itself is by adding a small imaginary term to the energy

$$[E \pm i\eta - H]\, G^{\mathrm{R/A}}(E) = I. \tag{2.46}$$

The definition of the retarded and advanced Green's function operators are now given by

$$G^{\mathrm{R}}(E) = \lim_{\eta \to 0^+} [E + i\eta - H]^{-1}, \tag{2.47}$$

$$G^{\mathrm{A}}(E) = \lim_{\eta \to 0^+} [E - i\eta - H]^{-1}. \tag{2.48}$$

Notice that the retarded (advanced) Green's function is analytic in the upper (lower) half of the complex plane. This definition holds for all energies. In the following sections only the retarded Green's function G^{R} will be used. To simplify the notation we will drop the subscript R, so that G stands for the retarded Green's function.

Using the Green's function, we can calculate the density of states (DOS), and the local tunneling density of states (LDOS) of a system

$$N(E) = -\frac{1}{\pi}\mathrm{Im}\left[\mathrm{Tr}\left[G(\mathbf{r},\mathbf{r}',E)\right]\right], \tag{2.49}$$

$$\rho(\mathbf{r},E) = -\frac{1}{\pi}\mathrm{Im}\left[G(\mathbf{r},\mathbf{r},E)\right]. \tag{2.50}$$

We now turn our attention to the actual calculation of the Green's function. Calculating the Green's function for an arbitrary continuous Hamiltonian of a conductor can be an extremely difficult task. To this end, a tight binding approximation is used to approximate the continuous Hamiltonian with a discrete lattice Hamiltonian. Using a finite discrete Hamiltonian to model the conductor, allows us to compute the Green's function using Eq. 2.47 by a simple matrix inversion. We will further discuss the tight binding model in Section 2.4.

Computing the Green's function of a conductor connected to semi-infinite leads is a more difficult task. While we can model any finite sized conductor using a tight binding model, trying the same method with a semi-infinite lead is impossible because the resulting matrix is infinite dimensional. The method we will use in this case is to compute the Green's function in several steps.

We can partition the overall Green's function into sub-matrices separating the leads from the conductor as follows (Eq. 2.43)

$$\begin{bmatrix} (E+i\eta)I - H_p & V_p \\ V_p^\dagger & (E+i\eta)I - H_\mathrm{C} \end{bmatrix} \begin{bmatrix} G_p & G_{p\mathrm{C}} \\ G_{\mathrm{C}p} & G_\mathrm{C} \end{bmatrix} \equiv 1, \tag{2.51}$$

where G_C is the conductors Green's function, G_p is Green's function for lead p, and V_p is the coupling potential between the conductor and lead p. H_p is the Hamiltonian for the isolated lead p and H_C is the Hamiltonian for the isolated conductor. The coupling potential V_p connects modes in lead p with sites on the conductor.

From Eq. 2.51 we can find an expression for G_C

$$G_\mathrm{C} = \left[(E+i\eta)I - H_\mathrm{C} - W_p^\dagger \frac{g_p}{\nu_0} W_p\right]^{-1}, \tag{2.52}$$

$$W_p = \sqrt{\nu_0} V_p, \tag{2.53}$$

where W_p is the coupling matrix and g_p is the retarded Green's function for the isolated lead p

$$g_p = \left[(E + i\eta)\, I - H_p\right]^{-1}. \tag{2.54}$$

The lead's Green's function g_p can often be calculated analytically. In this Thesis we will use normal leads and superconducting leads

$$g_{\mathrm{N}} = -i\pi\nu_0 I, \tag{2.55}$$

$$g_{\mathrm{SC}} = -i\pi\nu_0 \begin{pmatrix} \epsilon & 0 & 0 & \Delta \\ 0 & \epsilon & -\Delta & 0 \\ 0 & -\Delta^\star & \epsilon & 0 \\ \Delta^\star & 0 & 0 & \epsilon \end{pmatrix} \begin{cases} \frac{-1}{\sqrt{\epsilon^2 - |\Delta|^2}} & \epsilon < -|\Delta| \\ \frac{-i}{\sqrt{|\Delta|^2 - \epsilon^2}} & |\epsilon| < |\Delta| \\ \frac{1}{\sqrt{\epsilon^2 - |\Delta|^2}} & |\Delta| < \epsilon \end{cases}, \tag{2.56}$$

where the lead's Green's function are 4×4 matrices divided into particle-hole sectors, and further subdivided into spin up-spin down sectors.

The term $W_p^\dagger \frac{g_p}{\nu_0} W_p$ is called the retarded self energy term Σ_p^{R} for lead p. The self energy term arises from the interaction between the conductor and the leads, and it modifies the conductor Hamiltonian. When multiple independent leads are attached to the conductor, the self energies are added together

$$G_{\mathrm{C}} = \left[(E + i\eta)\, I - H_{\mathrm{C}} - \sum_p \Sigma_p^{\mathrm{R}}\right]^{-1}, \tag{2.57}$$

$$\Sigma_p^{\mathrm{R}} = W_p^\dagger \frac{g_p}{\nu_0} W_p. \tag{2.58}$$

Finally, we will use a known result to write the S-matrix in terms of the conductors Green's function G_{C}. This result is called the Weidenmüller formula

$$S = I - 2\pi i W G_{\mathrm{C}} W^\dagger. \tag{2.59}$$

The Weidenmüller formula together with the result for the Green's function (Eq.2.52) will allow us to numerically calculate the transmission function for an arbitrary finite conductor connected to semi-infinite leads. We will further elaborate on the tight binding method in Section 2.4.

2.4 Tight Binding Model and Simulation (the method of finite differences)

For the purpose of evaluating the Green's function of an arbitrarily shaped conductor, it would be useful to have a method that allows us to numerically evaluate it in a general fashion. In this chapter we will develop the method of finite differences, that aims to fulfill such requirements.

The method of finite differences is a technique to discretize the Hamiltonian of a continuous system. This is obtained by discretizing the Hamiltonian on a lattice. The lattice spacing is chosen such that it is smaller than the relevant physical parameters of the system, e.g. the Fermi wavelength. The lattice sites themselves do not necessarily correspond to an atom, but describe a region of the system in a coarse graining sense.

As we will later on see, the discretized Hamiltonians obtained using this method are similar to the tight-binding Hamiltonians widely used to model electronic transfer in molecules and condensed matter. Because of this similarity, the discretized Hamiltonians are commonly referred to as tight binding Hamiltonians and models. Although a misnomer, we will continue using this notation throughout the Thesis.

The method of tight binding is widely used today, and is a very useful tool in the calculation of physical quantities such as the transmission coefficients of the Landauer-Büttiker-Imry formulas. In this Thesis we will use this method in order to compute the visibility of a 1D semiconducting wire connected to an Aharonov-Bohm (AB) flux ring.

2.4.1 Semiconducting Nanowire Hamiltonian

We start with an extended version of the continuous 1D semiconducting wire Hamiltonian (Eq. 2.12), which includes here a Zeeman field in a general direction, and an additional electromagnetic vector potential $\mathbf{A}$. The Hamiltonian describes a spinful

electron in a 1D system moving along the y direction

$$H = \int dy\, \Psi^{\dagger}(y)\, \mathcal{H} \Psi(y), \tag{2.60}$$

$$\mathcal{H} = \frac{1}{2m^{\star}} \left(-i\hbar\nabla + e\mathbf{A}\right)^2 \tau_z - i\hbar\alpha\partial_y\sigma_z\tau_z + \mathbf{B}\cdot\boldsymbol{\sigma} + \Delta(y)\,\tau_x - \mu(y)\,\tau_z, \tag{2.61}$$

$$\Psi^{\dagger} = \left(\psi_{\uparrow}^{\dagger}, \psi_{\downarrow}^{\dagger}, \psi_{\downarrow}, -\psi_{\uparrow}\right), \tag{2.62}$$

where $m^{\star}$ and $-e$ are the effective mass and charge of the electron, $\psi_{\uparrow,(\downarrow)}(y)$ annihilates spin up (down) electrons at position y, α gives the Rashba spin-orbit coupling, $\mathbf{B}$ gives the Zeeman energy, Δ the induced superconductivity and μ the chemical potential. The Pauli matrices σ, τ operate in the spin and particle-hole space, respectively. In a strictly 1D system the vector potential term in the kinetic energy can be ignored.

The scheme for discretizing the Hamiltonian is as follows. First, a lattice is introduced with a lattice parameter a, this defines the points in the lattice $y = na$ where $n = 1, \ldots, N$. Each lattice creation operator is related to the continuous case by

$$\Psi_{\sigma}(y = na) \longrightarrow \frac{1}{\sqrt{a}} c_{n\sigma}. \tag{2.63}$$

The method of finite differences is used to approximate the derivative operators

$$\partial_x f(x) \longrightarrow \frac{1}{2a}\left[f(x+a) - f(x-a)\right], \tag{2.64}$$

$$\partial_{xx} f(x) \longrightarrow \frac{1}{a^2}\left[f(x+a) - 2f(x) + f(x-a)\right]. \tag{2.65}$$

To finish the procedure, all integrals are converted into sums

$$\int dy \longrightarrow a \sum_{\substack{y = na \\ n = 1, \ldots, N}}. \tag{2.66}$$

One can show that the Hamiltonian in Eq. 2.61 can be mapped onto a nearest

neighbor tight-binding Hamiltonian

$$H = \sum_{nss'} c^{\dagger}_{ns}\epsilon_{nss'}c_{ns'} + \left[c^{\dagger}_{ns}t_{nss'}c_{n+1,s'} + \text{h.c.}\right] + \sum_{n}\left[\Delta_n c^{\dagger}_{n\uparrow}c_{n\downarrow} + \text{h.c.}\right], \quad (2.67)$$

$$\epsilon_{nss'} = (2t - \mu_n)\,\delta_{ss'} + \mathbf{B}\cdot\boldsymbol{\sigma}, \quad (2.68)$$

$$t_{nss'} = -t\delta_{ss'} - iu\sigma^{z}_{ss'}, \quad (2.69)$$

where $t \equiv \frac{\hbar^2}{2ma^2}$, $u \equiv \frac{\alpha\hbar}{2a}$. The quantity $t_{nss'}$ gives the hopping amplitude between the sites of the wire, with the $-t\delta_{ss'}$ term originating from the kinetic term, and $-iu\sigma^{z}_{ss'}$ originating from the Rashba spin-orbit coupling term. The Rashba term adds an additional complex phase when hopping between sites.

2.4.2 Aharonov-Bohm Ring Hamiltonian

In an Aharonov-Bohm (AB) ring setup we have a 2D ring penetrated by a magnetic flux Φ. When describing a ring with a tight binding model, it is possible to use the previous formulation for a 1D model, but with an additional hopping term that connects the first site to the last site

$$H_{\text{T}} = t_{0,ss'}c^{\dagger}_{N,s}c_{1,s'} + \text{h.c.}, \quad (2.70)$$

where $t_{0,ss'}$ is given by Eq. 2.69.

The vector potential $\mathbf{A}$ now plays an important role in the Hamiltonian. The vector potential $\mathbf{A}$ along the wire is related to the AB flux Φ by

$$\Phi = \oint dl\, A\,(l)\,, \quad (2.71)$$

where the integral is taken around the ring of the circumference L. If we choose a gauge in which the vector potential is uniform around the ring, then

$$A\,(l) = \frac{\Phi}{L}. \quad (2.72)$$

Withing the chosen gauge, the hopping amplitude is modified using the Peierls

substitution [16]

$$\begin{aligned} t_{nss'} &\longrightarrow t_{nss'} \exp\left(i\tfrac{e}{\hbar}\int \overrightarrow{A}\cdot d\overrightarrow{l}\right) \\ &= t_{nss'} \exp\left(i\frac{2\pi}{N}\frac{\Phi}{\Phi_0}\right), \end{aligned} \tag{2.73}$$

where $\Phi_0 = {}^{h}\!/_{e}$

Notice that when considering 1D systems, we can always chose a gauge in which $\overrightarrow{A}$ is perpendicular to the wire, hence the magnetic field is gauged out. But when considering an AB flux ring, the geometry is no longer strictly 1D and we cannot ignore this term.

An alternative gauge exists, in which only one hopping term acquires a phase while all other terms remain unchanged

$$c_n \longrightarrow c_n \mathrm{e}^{-i(n-1/2)\frac{2\pi}{N}\frac{\Phi}{\Phi_0}}, \tag{2.74}$$

$$t' \longrightarrow t' \exp\left(2\pi i\frac{\Phi}{\Phi_0}\right). \tag{2.75}$$

This was the gauge of choice in this Thesis.

2.4.3 Proximity Coupling to a SC

When including the effects of superconductivity in a conductor Hamiltonian, the simplest method is to directly insert a superconducting pairing term into the tight binding Hamiltonian of the system $H \sim \Delta c^{\dagger}_{n\uparrow} c_{n\downarrow}$. This approach is useful when performing analytic calculations, as we will see later on in the thesis.

In our numerical simulations we will utilize a slightly different approach that is more precise. The system will be taken as a normal system that is tunnel coupled to SC leads [17]. In this case the pairing potential enters through the self energy term of the Green's function. In order to correctly model the effect of the proximity coupling of the SC we connect a different SC lead to each point. This gives each site a superconducting pairing term, without producing further unwanted interactions between sites. This also adds a small correction factor to the eigenenergies of the system. The self energy is obtained using Eq. 2.56, Eq. 2.58. The following self

energy term is created per site

$$\Sigma_{\mathrm{SC}} = -\pi\nu_{\mathrm{sc}} \left|t_{\mathrm{s}}\right|^2 \left(\frac{\epsilon I - \Delta\sigma_y\tau_y}{\sqrt{\left|\Delta\right|^2 - \epsilon^2}}\right), \tag{2.76}$$

with each site represented by a 4×4 matrix divided into particle-hole sectors, and further subdivided into spin up-spin down sectors. The Pauli matrices σ, τ operate in the spin and particle-hole space, respectively. Furthermore, ν_{sc} corresponds to the density of states of the bulk superconductor near the Fermi surface when $\Delta = 0$, and t_{s} is the hopping parameter between the wire and each SC lead. This term contains a correction to the energy levels of the system, and an additional SC pairing term which is energy dependent.

2.4.4 Modeling Experimental Systems

We wish to model a real experimental system using the above tight binding Hamiltonians. To do so we must perform a number of steps described here.

2.4.4.1 Tight Binding Parameters

We first relate the tight-binding parameters t, u, N to the physical parameters used in experiments. The spin-orbit coupling energy and the spin-orbit length are given respectively by

$$E_{\mathrm{SO}} = \frac{u^2}{t}, \tag{2.77}$$

$$l_{\mathrm{SO}} = a\frac{t}{u}, \tag{2.78}$$

where the lattice spacing is given by $a = \frac{L}{N}$, L is the length of the wire and N is the number of sites. Given E_{SO}, L and either $m^\star$ or l_{SO} we can compute all the tight binding parameters.

In order for the tight binding model to accurately describe its continuous counterpart, we require the bandwidth $4t$ to be larger than all other energy scales in the system. We first choose $4t \gg E_{\mathrm{SO}}, \Delta$. After choosing t, all other parameters a, N, u can be computed using the above equations.

As to the SC Δ_{ind} term, we have two options. If we directly inserted a Δ term into the conductors Hamiltonian, then $\Delta = \Delta_{\text{ind}}$. If we assumed the system is normal and is proximity coupled to SC leads, then assuming a hopping parameter t_s, and assuming small energies $\epsilon \ll \Delta_{\text{ind}}$ we have (Eq. 2.76)

$$\pi \nu_{\text{sc}} \left|t_{\text{s}}\right|^2 \approx \left|\Delta_{\text{ind}}\right|, \tag{2.79}$$

where Δ_{ind} is the induced SC pair potential.

2.4.4.2 Symmetrizing the Hamiltonian

The second step is to symmetrize the tight binding Hamiltonians in particle hole space by using the anticommutation relations and discarding the constant terms

$$c_{ns}^{\dagger} c_{ms'} = \frac{1}{2}\left(c_{ns}^{\dagger} c_{ms'} - c_{ms'} c_{ns}^{\dagger}\right) + \text{const.} \tag{2.80}$$

2.4.4.3 Writing the Hamiltonian in Matrix Form and Solving

The third step we write the Hamiltonians in matrix form using the Bogoliubov-De Gennes (BdG) formalism that includes particle-hole and spin up-down degrees of freedom

$$H = \sum_{n,m=1}^{4N} \Psi_m^{\dagger} \mathcal{H}_{mn}^{\text{BdG}} \Psi_n, \tag{2.81}$$

$$\Psi^{\dagger} = \left(c_{1\uparrow}^{\dagger},\ c_{1\downarrow}^{\dagger},\ \ldots\ c_{N\uparrow}^{\dagger},\ c_{N\downarrow}^{\dagger},\ c_{1\uparrow},\ c_{1\downarrow},\ \ldots\ c_{N\uparrow},\ c_{N\downarrow} \right). \tag{2.82}$$

The coupling matrix W from the Scattering matrix formula (Eq. 2.59) is a $4L \times 4N$ matrix, where L is the number of leads and each lead hosts 4 propagating channels: electron-hole, up-down. Each row represents a different channel in the lead, and each column represents a different creation operator on the different sites. Generally the

coupling Hamiltonian and coupling matrix are written as

$$\begin{aligned} H_{\mathrm{T}} &= \sum_{n,k,s} c_{ns}^{\dagger} t_{nks} a_{ks} + \mathrm{h.c.} \\ &= \sum_{n,s} \int dE\, \nu\left(E\right)\, c_{ns}^{\dagger} t_{ns}\left(E\right) a_{s}\left(E\right) + \mathrm{h.c.} \\ &= \int dE \Psi^{\dagger} W\left(E\right) \phi\left(E\right), \end{aligned} \tag{2.83}$$

$$\begin{aligned} \phi^{\dagger}\left(E\right) = \Big(& a_{1\uparrow}^{\dagger}\left(E\right), \;\; a_{1\downarrow}^{\dagger}\left(E\right), \;\; \ldots \;\; a_{L\uparrow}^{\dagger}\left(E\right), \;\; a_{L\downarrow}^{\dagger}\left(E\right), \\ & a_{1\uparrow}\left(E\right), \;\; a_{1\downarrow}\left(E\right), \;\; \ldots \;\; a_{L\uparrow}\left(E\right), \;\; a_{L\downarrow}\left(E\right) \Big), \end{aligned} \tag{2.84}$$

$$W_{ns}\left(E\right) = \sqrt{\nu\left(E\right)} t_{ns}\left(E\right), \tag{2.85}$$

where $\nu\left(E\right)$ is the density of states. The $\phi\left(E\right)$ matrix contains 4 channels for each lead at energy E, e.g. the terms $\sqrt{\nu\left(E\right)}\begin{pmatrix} a_{1\uparrow}^{\dagger} & a_{1\downarrow}^{\dagger} & a_{1\uparrow} & a_{1\downarrow} \end{pmatrix}$ represent the electron-hole up-down channels of the first lead at energy E.

Finally, we use the H and $W\left(E\right)$ matrices to obtain the scattering matrix S (Eq. 2.59) and compute the conductance and LDOS.

3 Analytic Calculations

In this chapter we will explore the theory behind the experimental setup proposed in Chapter 4. In the experiment we propose to measure the temperature dependence of the visibility $v(T)$ of an ABS and MBS. The visibility $v(T)$ at finite temperatures averages on processes of conductance including at zero energy and finite energy. Thus by measuring $v(T)$ we can gain an insight towards the zero energy conductance of a state, even at finite temperatures. In our calculations we concentrate on the effects of thermal smearing. We do not include de-phasing effects due to the increase of the thermal noise of the environment with temperature, we assume these effects are small.

We will demonstrate that the visibility of a MBS is a strictly increasing function of temperature, which tends to zero at zero temperature. While the visibility of an ABS can assume increasing, decreasing, constant or non-monotonic behavior. To prove this, we first start with an analytic expression for the temperature dependence of the zero bias conductance of a general Lorentzian conductance curve, which is known as a Breit-Wigner resonance. We use this expression to explore the visibility of such a state using a simple two valued model which assumes the maximal and minimal conductance toggles between two possible values.

We then write two simple analytic models, one for an isolated MBS and one for a zero bias ABS. Both models give a Breit-Wigner resonance. This will allow us to use the analytic expressions for conductance and visibility found for a general Breit-Wigner resonance, to prove the results for the ABS and MBS.

The results of this chapter will by used to interpret the results of the numerical simulation employed in Chapter 4.

3.1 Temperature Dependence of the Conductance

We start the analytic calculations by first developing an analytic formula for the temperature dependence of a conducting state. We will assume a general Breit-Wigner resonance, and see how it is affected by temperature. For this derivation, we use the temperature dependent Landauer-Büttiker-Imry formula (Eq. 2.35)

$$G(E,T) = \int_{-\infty}^{+\infty} G(\epsilon + E, T=0)\left(-\frac{\partial f_0}{\partial \epsilon}\right) d\epsilon, \tag{3.1}$$

$$G(E,T=0) = G_0 \frac{\Gamma^2}{E^2+\Gamma^2}. \tag{3.2}$$

This type of integral has a general solution [18]. If the integral can be expressed in the form

$$g(T) = \int_{-\infty}^{+\infty} g(\epsilon)\left(-\frac{\partial f_0}{\partial \epsilon}\right) d\epsilon, \tag{3.3}$$

$$g(\epsilon) = c + \sum_i \frac{r_i}{\epsilon - z_i}, \tag{3.4}$$

then $g(T)$ equals

$$g(T) = c - \sum_i \frac{r_i s_i}{2\pi i k T} \psi^{(1)}\left(\frac{1}{2} + \frac{s_i z_i}{2\pi i k T}\right), \tag{3.5}$$

with $s_i = \text{sign}(\text{Im}(z_i))$ and $\psi^{(m)}$ the polygamma function of order m.

The Lorentzian function (Eq. 3.2) can be expressed in the required form

$$G(\epsilon + E, T = 0) = \frac{G_0}{2}\left(\frac{i\Gamma}{\epsilon - (-E - i\Gamma)} - \frac{i\Gamma}{\epsilon - (-E + i\Gamma)}\right). \tag{3.6}$$

Which gives the result

$$G(E,T) = \frac{G_0}{2}\frac{\Gamma}{2\pi k T}\left(\psi^{(1)}\left(\frac{1}{2} + \frac{E + i\Gamma}{2\pi i k T}\right) + \psi^{(1)}\left(\frac{1}{2} + \frac{-E + i\Gamma}{2\pi i k T}\right)\right). \tag{3.7}$$

Looking at the zero bias conductance and defining $x = \frac{\Gamma}{2\pi k T}$, the equation assumes

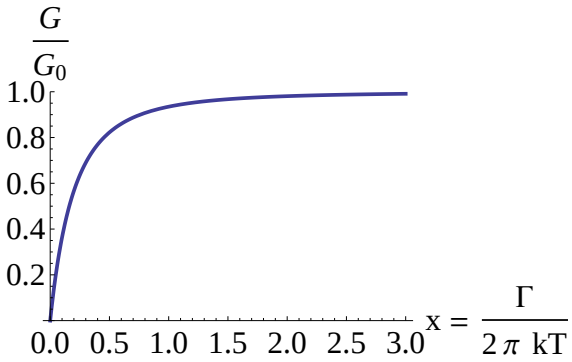

Figure 3.1: Plot of the zero bias conductance $G(E=0, x=\frac{\Gamma}{2\pi kT})$ (Eq. 3.8) of a Breit-Wigner resonance with width Γ and zero temperature conductance G_0.

a simpler form

$$G(E=0,x) = G_0\, x\, \psi^{(1)}\left(\frac{1}{2}+x\right). \tag{3.8}$$

$G(E=0,x)$ is a strictly increasing function of x (Fig. 3.1). Expanding Eq. 3.8 for high temperatures $\Gamma \ll kT \to x \ll 1$ we find

$$G(E=0,x\to 0) = G_0\left(\frac{\pi}{4}\frac{\Gamma}{kT} - \frac{7\zeta(3)}{2\pi^2}\left(\frac{\Gamma}{kT}\right)^2\right) + O\left[x^3\right], \tag{3.9}$$

where $\zeta(z)$ is the Riemann Zeta function.

In the low temperature limit $\Gamma \gg kT \to x \gg 1$ we have

$$G(E=0,x\to\infty) = G_0\left(1 - \frac{1}{3}\pi^2\left(\frac{kT}{\Gamma}\right)^2\right) + O\left[\frac{1}{x^3}\right]. \tag{3.10}$$

We can deduce from the monotonicity in x some straightforward statements. The first is that given constant zero temperature conductance ($G_0 = \text{const}$) and constant temperature ($T = \text{const}$), greater width results in larger conductance

$$\Gamma_1 > \Gamma_2 \Rightarrow G(E=0,G_0,\Gamma_1,T) > G(E=0,G_0,\Gamma_2,T). \tag{3.11}$$

The second is that given constant zero temperature conductance ($G_0 = \text{const}$) and constant width ($\Gamma = \text{const}$), greater temperature results in smaller conductance

$$T_1 > T_2 \Rightarrow G(E=0,G_0,\Gamma,T_1) < G(E=0,G_0,\Gamma,T_2). \tag{3.12}$$

From the linear dependence in the zero temperature conductance $G(E=0,x) \propto G_0$, we deduce that given constant temperature ($T = \text{const}$) and constant width ($\Gamma = \text{const}$), greater zero temperature conductance results in larger conductance at all temperatures

$$G_{0,1} > G_{0,2} \Rightarrow G\left(E=0, G_{0,1}, \Gamma, T\right) > G\left(E=0, G_{0,2}, \Gamma, T\right). \tag{3.13}$$

Finally, combining the linear dependence in the zero temperature conductance and the monotonicity in x, we deduce that given constant temperature ($T = \text{const}$), greater width and greater or equal zero temperature conductance results in larger conductance at all temperatures

$$\Gamma_1 > \Gamma_2, G_{0,1} \geq G_{0,2} \Rightarrow G\left(E=0, G_{0,1}, \Gamma_1, T\right) > G\left(E=0, G_{0,2}, \Gamma_2, T\right). \tag{3.14}$$

3.2 Temperature Dependence of the Visibility

In the AB experiment which we propose, we are interested in measuring the visibility of different conductance peaks as a function of temperature, denoted $v(T)$. In this section we will describe the different possible behaviors of $v(T)$.

In order to define the visibility, we assume that there is a physical parameter Φ that can be changed and will induce a periodic oscillation in the conductance as a function of that parameter.

$$G(\Phi) = G(L + \Phi), \tag{3.15}$$

where L is the period of oscillation. In the case of an AB experiment, this parameter is the magnetic flux passing through the ring section of the conductor. The visibility is defined by the maximal and minimal conductance $G_{\max}$, $G_{\min}$ measured in one oscillation period. In the previous section we have seen that the conductance changes as a function of temperature, this in turn causes a change in the visibility as a function of temperature

$$v(T) = \frac{G_{\max}(T) - G_{\min}(T)}{G_{\max}(T) + G_{\min}(T)}. \tag{3.16}$$

The visibility here is measured at $E = 0$, but can generally be measured at arbitrary

energy.

In order to better understand $v(T)$, we will explore the behavior of the visibility of a Breit-Wigner resonance. This will be useful later on when discussing the visibility of the MBS and ABS, because in the idealized case their conductance assumes a Breit-Wigner form.

3.2.1 Visibility of a Breit-Wigner Resonance

From Section 3.1, we know how a Breit-Wigner resonance is affected by temperature. For simplicity, we will assume that Φ keeps the shape of the Lorentzian intact, only changing Γ and G_0.

$$G(T,\Phi) = G_0(\Phi)\frac{\Gamma(\Phi)}{2\pi kT}\psi^{(1)}\left(\frac{1}{2}+\frac{\Gamma(\Phi)}{2\pi kT}\right). \tag{3.17}$$

In general, $\Gamma(\Phi)$ and $G_0(\Phi)$ can behave in any periodic fashion. For every temperature, we have $\Phi_{\min}(T)$, $\Phi_{\max}(T)$ that determine $G_{\max}(T)$, $G_{\min}(T)$. We emphasize that even though $\Gamma(\Phi)$, $G_0(\Phi)$ do not depend on temperature, $\Phi_{\min}(T)$ and $\Phi_{\max}(T)$ generally do depend on temperature and are determined by the exact nature of $\Gamma(\Phi)$, $G_0(\Phi)$. For simplicity, we will explore the behavior of $v(T)$ assuming $\Gamma(\Phi)$ and $G_0(\Phi)$ only toggle between two values

$$(\Gamma(\Phi), G_0(\Phi)) \in \{(\Gamma_1, G_{0,1}), (\Gamma_2, G_{0,2})\}. \tag{3.18}$$

Any visibility function in which $G_{\max}$, $G_{\min}$ do not depend on temperature is a subset of this model. We will see that this is the case for a MBS, which falls under Subsection 3.2.3. For an ABS, $G_{\max}(T)$, $G_{\min}(T)$ can assume a much more complicated behavior. But for the sake of demonstrating that an ABS can assume any different visibility behavior, the two value model will suffice. It is possible to engineer an ABS that falls into any of the following categories.

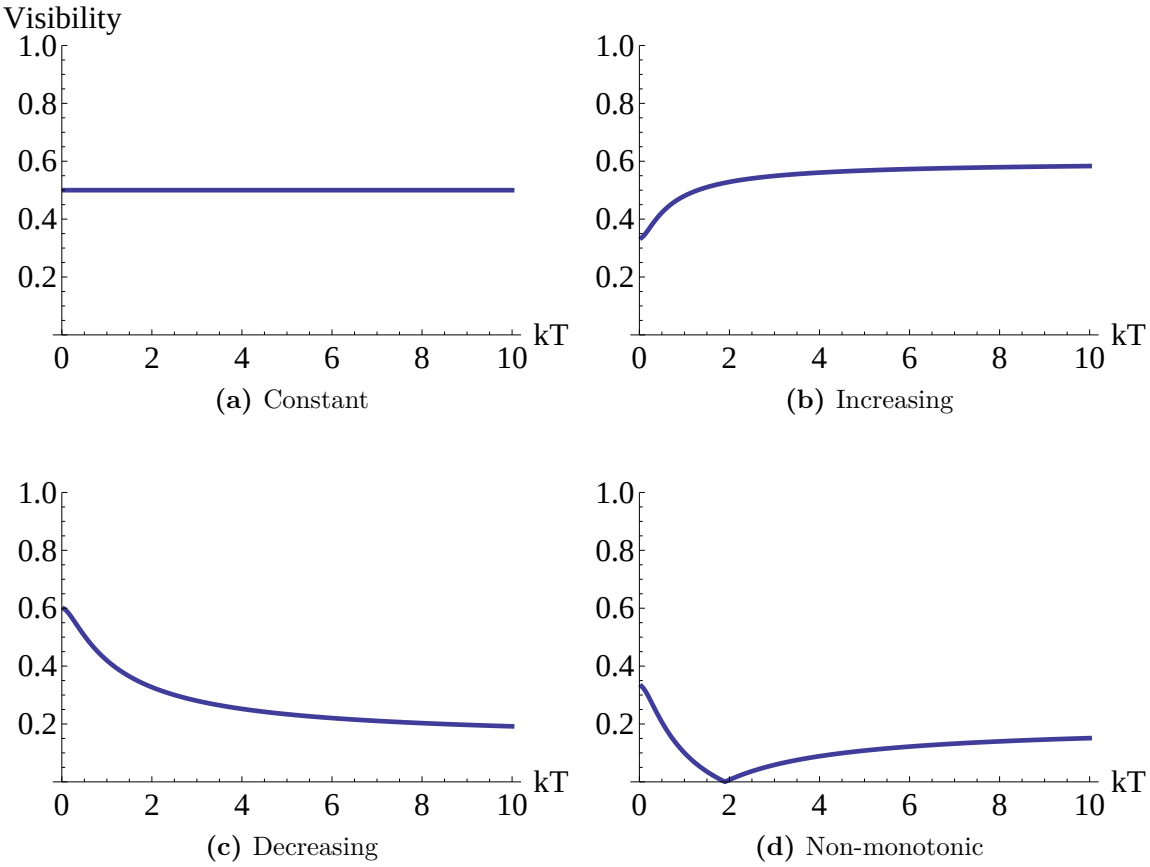

Figure 3.2: Examples of the different types of visibility behaviors for a simple two value $(\Gamma_1, G_{0,1})$, $(\Gamma_2, G_{0,2})$ model. (a) Constant visibility $\Gamma_1 = 3$, $G_{0,1} = 1$, $\Gamma_2 = 1$, $G_{0,2} = 1$. (b) Increasing visibility $\Gamma_1 = 2$, $G_{0,1} = 2$, $\Gamma_2 = 1$, $G_{0,2} = 1$. (c) Decreasing visibility $\Gamma_1 = 1$, $G_{0,1} = 3$, $\Gamma_2 = 4$, $G_{0,2} = 1$. (d) Non-monotonic visibility $\Gamma_1 = 1$, $G_{0,1} = 3$, $\Gamma_2 = 2$, $G_{0,2} = 1$.

3.2.2 Constant Visibility $\Gamma_1 = \Gamma_2$, $G_{0,1} \geq G_{0,2}$

From Eq. 3.13 we deduce that $G_{\max} = G(\Gamma_1, G_{0,1})$, $G_{\min} = G(\Gamma_2, G_{0,2})$,

$$v(T) = \frac{G_{0,1} - G_{0,2}}{G_{0,1} + G_{0,2}} = \text{const.} \tag{3.19}$$

The visibility is constant (Fig. 3.2a).

3.2.3 Increasing Visibility $\Gamma_1 > \Gamma_2$, $G_{0,1} \geq G_{0,2}$

From Eq. 3.14 we deduce that $G_{\max} = G(\Gamma_1, G_{0,1})$, $G_{\min} = G(\Gamma_2, G_{0,2})$

$$v(T) = \frac{\Gamma_1 G_{0,1}\left(\psi^{(1)}\left(\frac{\Gamma_1}{2\pi kT} + \frac{1}{2}\right)\right) - \Gamma_2 G_{0,2}\left(\psi^{(1)}\left(\frac{\Gamma_2}{2\pi kT} + \frac{1}{2}\right)\right)}{\Gamma_1 G_{0,1}\left(\psi^{(1)}\left(\frac{\Gamma_1}{2\pi kT} + \frac{1}{2}\right)\right) + \Gamma_2 G_{0,2}\left(\psi^{(1)}\left(\frac{\Gamma_2}{2\pi kT} + \frac{1}{2}\right)\right)}. \tag{3.20}$$

In the low temperature limit $\Gamma_1, \Gamma_2 \gg kT$:

$$v(T) \approx \frac{G_{0,1} - G_{0,2}}{G_{0,1} + G_{0,2}} + \frac{2\pi^2}{3} \frac{G_{0,1} G_{0,2}}{(G_{0,1} + G_{0,2})^2} \left(\frac{1}{\Gamma_2^2} - \frac{1}{\Gamma_1^2}\right) (kT)^2. \tag{3.21}$$

In the high temperature limit $\Gamma_1, \Gamma_2 \ll kT$:

$$v(T) \approx \frac{G_{0,1}\Gamma_1 - G_{0,2}\Gamma_2}{G_{0,1}\Gamma_1 + G_{0,2}\Gamma_2} - \frac{28\zeta(3)}{\pi^3} \frac{G_{0,1}\Gamma_1 G_{0,2}\Gamma_2 (\Gamma_1 - \Gamma_2)}{(G_{0,1}\Gamma_1 + G_{0,2}\Gamma_2)^2} \frac{1}{kT}, \tag{3.22}$$

where $\zeta(z)$ is the Riemann Zeta function. From these limits it is easy to see that

$$v(T \to 0) < v(T \to \infty). \tag{3.23}$$

Overall the visibility is a strictly increasing function of T (Fig. 3.2b).

3.2.4 Decreasing and Non-Monotonic Visibility $\Gamma_1 > \Gamma_2$, $G_{0,1} < G_{0,2}$

Figuring which points determine $G_{\max}(T)$, $G_{\min}(T)$ depends on the parameters of the problem. This determines the visibility, which can be decreasing or non-monotonic.

In the low temperature limit, $\Gamma_1, \Gamma_2 \gg kT$, the minimal and maximal conductance $G_{\min}$, $G_{\max}$ are easily determined by using Eq. 3.10

$$G_{\min} = G(T, \Gamma_1, G_{0,1}) \to G_{0,1}, \tag{3.24}$$
$$G_{\max} = G(T, \Gamma_2, G_{0,2}) \to G_{0,2}. \tag{3.25}$$

The visibility in the low temperature limit is given by

$$v(T) \approx \frac{G_{0,2} - G_{0,1}}{G_{0,2} + G_{0,1}} - \frac{2\pi^2}{3} \frac{G_{0,1} G_{0,2}}{(G_{0,1} + G_{0,2})^2} \left(\frac{1}{\Gamma_2^2} - \frac{1}{\Gamma_1^2} \right) (kT)^2 . \tag{3.26}$$

In the high temperature limit, $\Gamma_1, \Gamma_2 \ll kT$, we use Eq. 3.9 and get an expression for the conductance

$$G(T, \Gamma_1, G_{0,1}) \approx \frac{\pi}{4} \Gamma_1 G_{0,1} \frac{1}{kT}, \tag{3.27}$$
$$G(T, \Gamma_2, G_{0,2}) \approx \frac{\pi}{4} \Gamma_2 G_{0,2} \frac{1}{kT}. \tag{3.28}$$

The behavior of the visibility function is split into two cases. In the case that $\Gamma_1 G_{0,1} \leq \Gamma_2 G_{0,2}$, we have

$$G_{\min} = G(T, \Gamma_1, G_{0,1}), \tag{3.29}$$
$$G_{\max} = G(T, \Gamma_2, G_{0,2}), \tag{3.30}$$

with the visibility in the high temperature limit given by

$$v(T) \approx \frac{G_{0,2}\Gamma_2 - G_{0,1}\Gamma_1}{G_{0,2}\Gamma_2 + G_{0,1}\Gamma_1} + \frac{28\zeta(3)}{\pi^3} \frac{G_{0,1}\Gamma_1 G_{0,2}\Gamma_2 (\Gamma_1 - \Gamma_2)}{(G_{0,1}\Gamma_1 + G_{0,2}\Gamma_2)^2} \frac{1}{kT}. \tag{3.31}$$

It is easy to see that

$$v(T \to 0) > v(T \to \infty), \tag{3.32}$$

and deduce that the visibility is a strictly decreasing function of T (Fig. 3.2c).

In the case that $\Gamma_1 G_{0,1} > \Gamma_2 G_{0,2}$, we have

$$G_{\min} = G\left(T, \Gamma_2, G_{0,2}\right), \tag{3.33}$$
$$G_{\max} = G\left(T, \Gamma_1, G_{0,1}\right), \tag{3.34}$$

with the visibility in the high temperature limit given by

$$v\left(T\right) \approx \frac{G_{0,1}\Gamma_1 - G_{0,2}\Gamma_2}{G_{0,1}\Gamma_1 + G_{0,2}\Gamma_2} - \frac{28\zeta\left(3\right)}{\pi^3} \frac{G_{0,1}\Gamma_1 G_{0,2}\Gamma_2 \left(\Gamma_1 - \Gamma_2\right)}{\left(G_{0,1}\Gamma_1 + G_{0,2}\Gamma_2\right)^2} \frac{1}{kT}. \tag{3.35}$$

In this case the visibility is non-monotonic (Fig. 3.2d). Initially $G_{\min} = G\left(T, \Gamma_1, G_{0,1}\right)$, $G_{\max} = G\left(T, \Gamma_2, G_{0,2}\right)$ and the visibility decreases. From a certain point the two points exchange roles $G_{\min} = G\left(T, \Gamma_2, G_{0,2}\right)$, $G_{\max} = G\left(T, \Gamma_1, G_{0,1}\right)$ and the visibility increases. This case is interesting because it shows an example of non-monotonic visibility and non constant $\Phi_{\min}\left(T\right)$, $\Phi_{\max}\left(T\right)$ for a relatively simple model.

3.3 Simple Analytic Model

The aim of this section is to gain a basic understanding of the theory behind the experimental setup and the numerical simulations detailed in Chapter 4. In the simulation we will explore the visibility as a function of temperature for the proposed setup. We will achieve an understanding of the system by deriving analytic expressions for the temperature dependence of the visibility of a ZBCP in systems hosting a MBS or an ABS. We will demonstrate that the visibility of a MBS is a strictly increasing function of temperature, while the visibility of an ABS can assume increasing, decreasing, constant or non-monotonic behavior.

3.3.1 Conductance of a MBS

Assume a general low-energy model of a normal lead coupled to a MBS [19]. The most general Hamiltonian describing such a system is

$$H = H_{\mathrm{L}} + H_{\mathrm{MBS}} + H_{\mathrm{T}}, \tag{3.36}$$

where H_{L} is the normal lead Hamiltonian, H_{MBS} is the MBS Hamiltonian and H_{T} couples between the lead and the MBS. The lead Hamiltonian is given by

$$H_{\mathrm{L}} = \sum_{k,s} \epsilon_k \psi_{ks}^{\dagger} \psi_{ks}, \tag{3.37}$$

where $\psi_{ks}^{\dagger}$, ψ_{ks} are the creation and annihilation operators of an electron in a lead mode with momentum k, spin s and energy ϵ_k.

The Hamiltonian H_{MBS} is assumed to consists of two spatially separated zero energy MBS, and a superconducting energy gap. The distance between the MBS needs to be large enough so that there is no overlap between the two. An overlap will cause an unwanted splitting of energies from zero to a finite value. Given these assumptions and the restriction to low energies, we discard any excitations above the gap, leaving only the two spatially separated zero energy MBS γ_1,γ_2. The Hamiltonian is reduced to

$$H_{\mathrm{MBS}} = 0. \tag{3.38}$$

By assumption, the coupling Hamiltonian connects the states in the lead to one of the MBS, which we will generally denote as γ. The coupling Hamiltonian is given by

$$\begin{aligned} H_{\mathrm{T}} &= \sum_{k,s} \left((it_{\mathrm{s}}) \gamma^{\dagger} \psi_{k,s} + \mathrm{h.c.} \right) \\ &= i\gamma \sum_{k,s} \left(t_{\mathrm{s}} \psi_{k,s} + \mathrm{h.c.} \right). \end{aligned} \tag{3.39}$$

We now write the scattering matrix of the system. We are interested only in the low energy dynamics that occur below the superconducting gap, in this case only reflection processes are allowed [20]. This allows us to write only the S-matrix of the reflection into the normal lead, and infer from it the observables of interest. The scattering matrix is given by (Eq. 2.59)

$$S = \begin{pmatrix} r^{ee} & r^{eh} \\ r^{he} & r^{hh} \end{pmatrix} = I - 2\pi i W^{\dagger} \left(E \cdot I + H_{\mathrm{MBS}} + i\pi W W^{\dagger} \right)^{-1} W, \tag{3.40}$$

with $W = i\sqrt{\nu_0} \left(t_{\uparrow}, t_{\downarrow}, t_{\uparrow}^{*}, t_{\downarrow}^{*} \right)$, and ν_0 being the density of states in the normal lead.

This gives

$$r^{ee}_{ss'} = \delta_{ss'} + \frac{2\pi\nu_0 t^*_s t_{s'}}{iE-\Gamma}, \tag{3.41}$$

$$r^{he}_{ss'} = \frac{2\pi\nu_0 t_s t_{s'}}{iE-\Gamma}, \tag{3.42}$$

$$\Gamma = 2\pi\nu_0\left(|t_\uparrow|^2 + |t_\downarrow|^2\right). \tag{3.43}$$

By applying the particle hole symmetry operator $\Xi = \tau_x \otimes I_{2\times2} \cdot K$ (τ operates on the particle hole space, $I_{2\times2}$ on spin space, K is the complex conjugation operator) on the scattering matrix we see that $r^{hh}(E) = [r^{ee}(-E)]^*$, $r^{eh}(E) = \left[r^{he}(-E)\right]^*$. Using this symmetry we can write the conductance as [21]

$$G(E) = \frac{2e^2}{h}\mathrm{Tr}\left[I - r^{ee}\left(r^{ee}\right)^\dagger + r^{he}\left(r^{he}\right)^\dagger\right], \tag{3.44}$$

$$G_{\mathrm{MBS}}(E) = \frac{2e^2}{h}\frac{\Gamma^2}{E^2+\Gamma^2}. \tag{3.45}$$

From this simple expression we see that $G_{\mathrm{MBS}}(E=0)$ always equals $\frac{2e^2}{h}$. This is a general attribute of conductance through a MBS in an infinite system. The width is 2Γ and depends on the details of the problem.

3.3.2 Visibility of a MBS

We now add the effect of an Aharonov-Bohm ring (Subsection 2.4.2) between the lead and the MBS. For simplicity, we only include the leading order $\frac{\Phi}{\Phi_0}$ effect of a particle passing once through the upper loop or once through the lower loop. Higher order $N\frac{\Phi}{\Phi_0}$ ($N \geq 2$) effects that include further windings around the loop are ignored. We also assume that thermal smearing and de-phasing along the ring arm are negligible. This gives a simple modification of the original conductance expressions (Eq. 3.43, Eq. 3.45)

$$t_\uparrow \rightarrow t_{\uparrow1} + t_{\uparrow2}\mathrm{e}^{2\pi i\frac{\Phi}{\Phi_0}}, \tag{3.46}$$

$$t_\downarrow \rightarrow t_{\downarrow1} + t_{\downarrow2}\mathrm{e}^{2\pi i\frac{\Phi}{\Phi_0}}, \tag{3.47}$$

$$\Gamma = 2\pi\nu_0\left(\left|t_{\uparrow1} + t_{\uparrow2}\mathrm{e}^{2\pi i\frac{\Phi}{\Phi_0}}\right|^2 + \left|t_{\downarrow1} + t_{\downarrow2}\mathrm{e}^{2\pi i\frac{\Phi}{\Phi_0}}\right|^2\right). \tag{3.48}$$

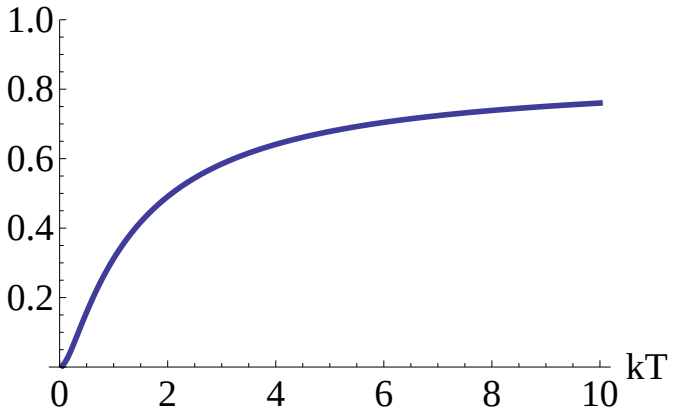

Figure 3.3: Example of the MBS visibility function, which is a monotonically increasing function of temperature, that equals zero at zero temperature. $t_{\uparrow 1} = 1$, $t_{\uparrow 2} = 2$, $t_{\downarrow 1} = 1$, $t_{\downarrow 2} = 1$.

The zero temperature conductance of a MBS is a Lorentzian curve. Changing the magnetic flux keeps the zero bias conductance G_0 constant, while changing the width of the curve. We expect that if the AB ring has any effect on the system, the width of the conductance will change with Φ, giving a maximal and minimal width $\Gamma_{\max}$, $\Gamma_{\min}$.

In Section 3.2 we have analyzed the temperature dependence of the visibility of such a state. The MBS falls into the category described in Subsection 3.2.3. This means that the visibility of the MBS in our setup is a strictly increasing function of temperature

$$v_{\mathrm{MBS}}(T) = \frac{\Gamma_{\max}\psi^1\left(\frac{\Gamma_{\max}}{2\pi kT}+\frac{1}{2}\right) - \Gamma_{\min}\psi^1\left(\frac{\Gamma_{\min}}{2\pi kT}+\frac{1}{2}\right)}{\Gamma_{\max}\psi^1\left(\frac{\Gamma_{\max}}{2\pi kT}+\frac{1}{2}\right) + \Gamma_{\min}\psi^1\left(\frac{\Gamma_{\min}}{2\pi kT}+\frac{1}{2}\right)}. \tag{3.49}$$

Furthermore, because $G_{\max} = G_{\min}$ then $v(T \to 0) = 0$ (Fig. 3.3).

In the high temperature limit $\Gamma_{\max}, \Gamma_{\min} \ll kT$,

$$v_{\mathrm{MBS}}(T) \approx \frac{\Gamma_{\max} - \Gamma_{\min}}{\Gamma_{\max} + \Gamma_{\min}} - \frac{28\zeta(3)}{\pi^3}\frac{\Gamma_{\max}\Gamma_{\min}(\Gamma_{\max} - \Gamma_{\min})}{(\Gamma_{\max} + \Gamma_{\min})^2}\frac{1}{kT}. \tag{3.50}$$

In the low temperature limit $\Gamma_{\max}, \Gamma_{\min} \gg kT$,

$$v_{\mathrm{MBS}}(T) \approx \frac{\pi^2}{6}\left(\frac{1}{\Gamma_{\min}^2} - \frac{1}{\Gamma_{\max}^2}\right)(kT)^2. \tag{3.51}$$

The model developed above does not depend on the details of the particular system hosting the MBS, the AB ring, or the nature of the coupling between the lead and system. As long as the system hosts two infinitely separated zero bias Majorana bound states and an energy gap, the results obtained above should hold.

3.3.3 Conductance of a Zero Bias ABS

In this section we consider an accidental zero energy ABS. We want to show that in this case the visibility can assume many different behaviors, namely: constant, increasing, decreasing or non-monotonic behavior. In order to show this, we will confine ourselves to a simple model which conserves spin in the z direction. This will be enough to obtain a tunable Breit-Wigner resonance and will allow us to demonstrate the basic behaviors of visibility discussed in Subsection 3.2.1. More elaborate models can exhibit more complicated behaviors, but this is not needed for our needs.

The model consists of a single level quantum dot with a Zeeman field, coupled to a superconducting lead and a normal lead [19]. As in the MBS case, we deal only with energies smaller than the superconducting gap, allowing us to write only the S-matrix of the normal lead. The superconducting degrees of freedom will be integrated out by absorbing the superconducting lead self energy term into the dot Hamiltonian. We are interested in a low energy theory, thus excitations above the superconducting gap (Bogoliubov quasiparticles) will be ignored.

These considerations lead to the following effective low energy Hamiltonian

$$
\begin{aligned}
H &= H_{\mathrm{L}} + H_{\mathrm{D}} + H_{\mathrm{T}}, && (3.52)\\
H_{\mathrm{L}} &= \sum_{k,s} \epsilon_k \psi^{\dagger}_{ks} \psi_{ks}, && (3.53)\\
H_{\mathrm{D}} &= \sum_{ss'} \left(\epsilon_0 \delta_{ss'} + B\sigma^{z}_{ss'}\right) d^{\dagger}_{s} d_{s'} + \left(\bar{\Delta} d^{\dagger}_{\uparrow} d^{\dagger}_{\downarrow} + \mathrm{h.c.}\right), && (3.54)\\
H_{\mathrm{T}} &= \sum_{ks} w_s \psi^{\dagger}_{ks} d_s + \mathrm{h.c.}, && (3.55)
\end{aligned}
$$

where H_{L} is the lead Hamiltonian, H_{D} is the dot Hamiltonian and H_{T} is the coupling Hamiltonian. The operators $\psi^{\dagger}_{ks}$, ψ_{ks} are the creation and annihilation operators of an electron in a lead mode with momentum k and spin s, $d^{\dagger}_{s}$ and d_s create and annihilate a spin s electron on the dot, ϵ_0 is the energy level of an isolated quantum

dot, B is the Zeeman field, and $\bar{\Delta}$ is the effective induced pair potential in the dot. In order to conserve σ_z, the Zeeman field B points towards the z axis. We assume that we can ignore any Coulomb blockade effects i.e. that the charging energy is much smaller than $\bar{\Delta}$. Diagonalizing H_{D} gives

$$\begin{aligned} H_{\mathrm{D}} &= \left(\sqrt{\epsilon_0^2+\bar{\Delta}^2}-B\right)a^\dagger a+\left(\sqrt{\epsilon_0^2+\bar{\Delta}^2}+B\right)b^\dagger b+\text{const}, && (3.56)\\ a &= \sin(\alpha)\,d_\uparrow^\dagger-\cos(\alpha)\,d_\downarrow, && (3.57)\\ b &= \cos(\alpha)\,d_\uparrow+\sin(\alpha)\,d_\downarrow^\dagger, && (3.58)\\ \cos(2\alpha) &= \frac{\epsilon_0}{\sqrt{\epsilon_0^2+\bar{\Delta}^2}}. && (3.59)\end{aligned}$$

Tuning the Zeeman energy B to the value $B=\sqrt{\epsilon_0^2+\bar{\Delta}^2}$ leads to the formation of an ABS with zero energy.

The dot Hamiltonian, H_{D}, is now composed of two components. A zero energy $a^\dagger$ excitation, and a high energy $b^\dagger$ excitation. Projecting our Hamiltonian into the low energy subspace results in

$$\begin{aligned} H_{\mathrm{D}} &= 0, && (3.60)\\ H_{\mathrm{T}} &= \sum_{ks} a\left(w_\uparrow^*\sin(\alpha)\,\psi_{k\uparrow}+w_\downarrow\cos(\alpha)\,\psi_{k\downarrow}^\dagger\right)+\text{h.c.} && (3.61)\\ &= \sum_{ks} a\left(\widetilde{t}_\uparrow\psi_{k\uparrow}+\widetilde{t}_\downarrow^*\psi_{k\downarrow}^\dagger\right)+\text{h.c.}, && (3.62)\end{aligned}$$

with $\widetilde{t}_\uparrow=w_\uparrow^*\sin(\alpha)$, $\widetilde{t}_\downarrow^*=w_\downarrow\cos(\alpha)$. Writing the scattering matrix using Eq. 2.59 and the coupling matrix

$$W=\sqrt{\nu_0}\begin{pmatrix}\widetilde{t}_\uparrow & 0 & 0 & \widetilde{t}_\downarrow^*\\ 0 & \widetilde{t}_\downarrow & \widetilde{t}_\uparrow^* & 0\end{pmatrix}, \qquad (3.63)$$

allows us to obtain the reflection matrices

$$r^{ee}_{ss'} = \frac{iE}{iE - \widetilde{\Gamma}/2}\delta_{ss'} + \frac{(\widetilde{\Gamma}_\uparrow - \widetilde{\Gamma}_\downarrow)/2}{iE - \widetilde{\Gamma}/2}\sigma^z_{ss'}, \tag{3.64}$$

$$r^{he}_{ss'} = \frac{2\pi\nu_0 \widetilde{t}_\uparrow \widetilde{t}_\downarrow}{iE - \widetilde{\Gamma}/2}\sigma^x_{ss'}, \tag{3.65}$$

$$\widetilde{\Gamma}_{\uparrow/\downarrow} = 2\pi\nu_0 \left|\widetilde{t}_{\uparrow/\downarrow}\right|^2, \tag{3.66}$$

$$\widetilde{\Gamma} = \widetilde{\Gamma}_\downarrow + \widetilde{\Gamma}_\uparrow. \tag{3.67}$$

Using Eq. 3.44 we find the conductance

$$G_{\mathrm{ABS}} = G_{0,\mathrm{ABS}} \frac{\left(\widetilde{\Gamma}/2\right)^2}{E^2 + \left(\widetilde{\Gamma}/2\right)^2}, \tag{3.68}$$

which at $E = 0$ gives

$$G_{0,\mathrm{ABS}} = \frac{4e^2}{h}\frac{\widetilde{\Gamma}_\downarrow \widetilde{\Gamma}_\uparrow}{\left(\widetilde{\Gamma}/2\right)^2} \leq \frac{4e^2}{h}. \tag{3.69}$$

From this expression we see that the conductance is a Lorentzian curve where both $G_{\mathrm{ABS}}(E = 0)$ and the width depend on the details of the model parameters.

3.3.4 Visibility of a Zero Bias ABS

As in Subsection 3.3.2, we add to the conductance (Eq. 3.68) the effect of an AB ring (Eq. 3.46, Eq. 3.47)

$$\widetilde{\Gamma} = 2\pi\nu_0 \left(\left| \widetilde{t}_{\uparrow 1} + \widetilde{t}_{\uparrow 2} \mathrm{e}^{2\pi i \frac{\Phi}{\Phi_0}} \right|^2 + \left| \widetilde{t}_{\downarrow 1} + \widetilde{t}_{\downarrow 2} \mathrm{e}^{2\pi i \frac{\Phi}{\Phi_0}} \right|^2 \right) \tag{3.70}$$

$$G_{0,\mathrm{ABS}} = \frac{4e^2}{h} \frac{2 \left| \widetilde{t}_{\uparrow 1} + \widetilde{t}_{\uparrow 2} \mathrm{e}^{2\pi i \frac{\Phi}{\Phi_0}} \right|^2 \left| \widetilde{t}_{\downarrow 1} + \widetilde{t}_{\downarrow 2} \mathrm{e}^{2\pi i \frac{\Phi}{\Phi_0}} \right|^2}{\left(\left| \widetilde{t}_{\uparrow 1} + \widetilde{t}_{\uparrow 2} \mathrm{e}^{2\pi i \frac{\Phi}{\Phi_0}} \right|^2 + \left| \widetilde{t}_{\downarrow 1} + \widetilde{t}_{\downarrow 2} \mathrm{e}^{2\pi i \frac{\Phi}{\Phi_0}} \right|^2 \right)} \tag{3.71}$$

As discussed in the beginning of the chapter, we wish to demonstrate that the visibility of a zero bias ABS can assume many different behaviors. This can be

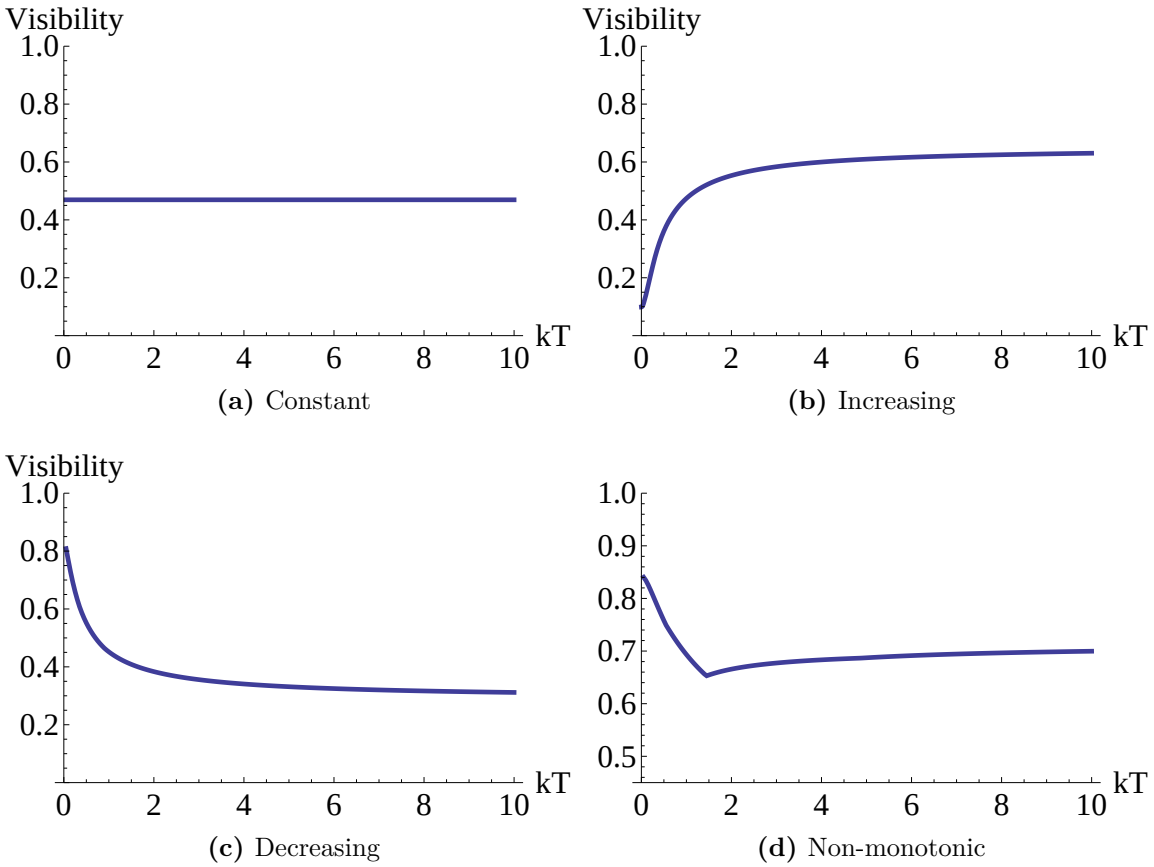

Figure 3.4: Examples of the different types of visibility behaviors for a simple zero bias ABS model where σ^z is conserved. (a) Constant visibility $\widetilde{t}_{\uparrow 1} = -1$, $\widetilde{t}_{\uparrow 2} = 0.5$, $\widetilde{t}_{\downarrow 1} = 1$, $\widetilde{t}_{\downarrow 2} = 0.5$. (b) Increasing visibility $\widetilde{t}_{\uparrow 1} = 1$, $\widetilde{t}_{\uparrow 2} = 0.5$, $\widetilde{t}_{\downarrow 1} = 1$, $\widetilde{t}_{\downarrow 2} = 0.2$. (c) Decreasing visibility $\widetilde{t}_{\uparrow 1} = 0.05$, $\widetilde{t}_{\uparrow 2} = -0.25$, $\widetilde{t}_{\downarrow 1} = 0.5$, $\widetilde{t}_{\downarrow 2} = 1$. (d) Non-monotonic visibility $\widetilde{t}_{\uparrow 1} = 0.2$, $\widetilde{t}_{\uparrow 2} = -0.6$, $\widetilde{t}_{\downarrow 1} = 1.25$, $\widetilde{t}_{\downarrow 2} = 1.45$.

shown by plotting the visibility using different $\widetilde{t}_{\uparrow 1}$, $\widetilde{t}_{\uparrow 2}$, $\widetilde{t}_{\downarrow 1}$, $\widetilde{t}_{\downarrow 2}$ parameters. The different cases here are:

a) Constant visibility $\widetilde{t}_{\uparrow 1} = -1$, $\widetilde{t}_{\uparrow 2} = 0.5$, $\widetilde{t}_{\downarrow 1} = 1$, $\widetilde{t}_{\downarrow 2} = 0.5$ (Fig. 3.4a).

b) Increasing visibility $\widetilde{t}_{\uparrow 1} = 1$, $\widetilde{t}_{\uparrow 2} = 0.5$, $\widetilde{t}_{\downarrow 1} = 1$, $\widetilde{t}_{\downarrow 2} = 0.2$ (Fig. 3.4b).

c) Decreasing visibility $\widetilde{t}_{\uparrow 1} = 0.05$, $\widetilde{t}_{\uparrow 2} = -0.25$, $\widetilde{t}_{\downarrow 1} = 0.5$, $\widetilde{t}_{\downarrow 2} = 1$ (Fig. 3.4c).

d) Non-monotonic visibility $\widetilde{t}_{\uparrow 1} = 0.2$, $\widetilde{t}_{\uparrow 2} = -0.6$, $\widetilde{t}_{\downarrow 1} = 1.25$, $\widetilde{t}_{\downarrow 2} = 1.45$ (Fig. 3.4d).

3.4 Conclusion

In this chapter we have proven a necessary but not sufficient condition for experimentally identifying MBSs. In an experiment we should connect an AB ring to our wire and measure the visibility of the conducting state as a function of temperature. We have seen that we can classify conductance peaks by their visibility. A MBS necessarily has visibility that increases with the temperature, while an ABS can assume several different behaviors. This allows us to exclude the existence of a MBS if the visibility of the conducting state exhibits any behavior that is not strictly increasing. In case of a MBS, the increasing visibility is a robust character of the system and should not depend on details such as additional disorder or coupling strength.

4 Numerical Calculations and Results

Following the analytical results of Chapter 3, we now have a simple experimental tool that can help us determine if a system hosts a MBS. The idea is to connect a wire that has a MBS at its ends to a normal lead that has an AB ring attached to it, and to measure the zero bias visibility as a function of temperature. In a system that hosts well separated MBSs, we expect the visibility to be a strictly increasing function of temperature, which tends to zero at zero temperature. If the visibility does not exhibit this behavior, we can rule out the possibility of well separated MBSs.

To strengthen the analytic results, we will now report on a numerical simulation of an experimentally realizable system, and see that the visibility indeed acts as expected. We consider a system used in recent experiments which consists of a 1D nanowire with Rashba spin-orbit coupling and a Zeeman field, proximity coupled to an s-wave superconductor [8, 9, 10, 22]. In these experiments, emphasis was made on measuring a ZBCP, which is consistent with the presence of a MBS. While this indication might seem unique, other mechanisms have been proposed that mimic this behavior in the absence of a MBS [11, 12, 17, 23, 24, 25]. Thus it is crucial to posses further indications for the presence of a MBS.

In this chapter we will present a tight binding simulation of a system (Fig. 4.1) consisting of a 1D nanowire with properties mentioned above. The wire is connected to a normal lead with an attached AB flux ring. We will show that the wire can host several different states which exhibit a ZBCP, but not all corresponding to a topological state with a MBS. We will be able to distinguish between them using the dependence of the visibility on the temperature.

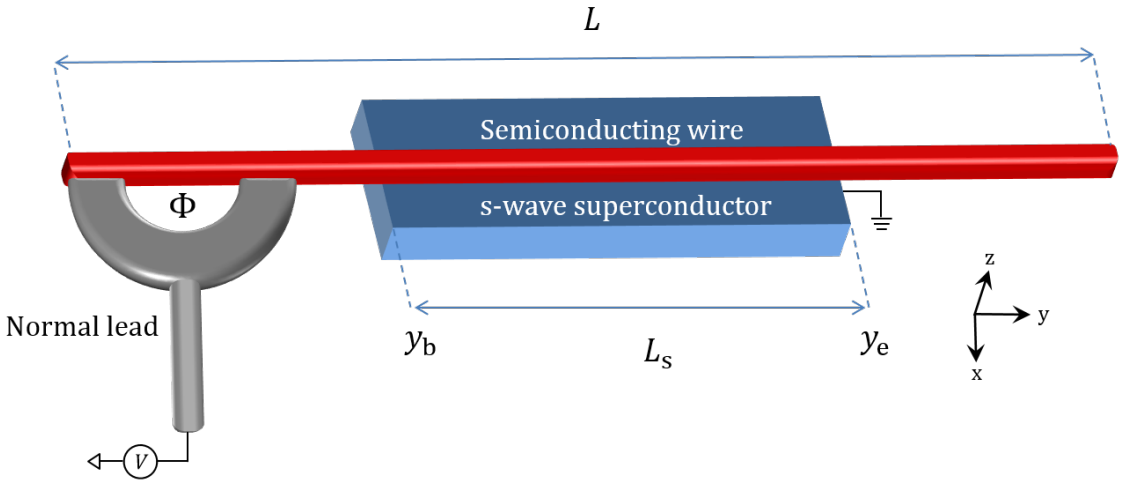

Figure 4.1: Experimental setup. A semiconducting 1D nanowire proximity coupled to an s-wave superconducting lead. The system can be tuned to host Majorana bound states (MBS) at its ends in the topological phase. In the non-topological phase the system can be tuned to host a zero energy Andreev bound state (ABS). A normal lead is connected to the left. The normal lead and part of the wire form an Aharonov-Bohm flux ring. We measure the visibility as a function of temperature. In the topological phase, when the system hosts well separated MBSs, we expect the visibility to be a strictly increasing function of temperature, which tends to zero at zero temperature. While for a low energy non-topological Andreev bound state the visibility can assume increasing, decreasing, constant or non-monotonic behavior.

4.1 Tight Binding Simulation

We present a tight binding simulation (Section 2.4) of a 1D nanowire with Rashba spin-orbit coupling and a Zeeman field, proximity coupled to an s-wave superconductor (Fig. 4.1). The wire is tunnel coupled from the left to a normal lead through an AB ring. To correctly simulate the effects of proximity coupling, we connect a SC lead (Subsection 2.4.3) to the mid section of the wire between $y_\mathrm{b} \leq y \leq y_\mathrm{e}$. Since the Fermi wavelength in the superconductor is much shorter than the one in the semiconductor (that we simulate as a set of discrete sites) we may neglect cross Andreev reflections between adjacent sites of the tight binding model.

The Hamiltonian for the system is $H = H_\mathrm{nw} + H_\mathrm{L,N} + H_\mathrm{L,SC} + H_\mathrm{T,N} + H_\mathrm{T,SC}$ with $H_\mathrm{L,N}$, $H_\mathrm{L,SC}$ the Hamiltonians of the normal and SC leads, H_nw the Hamiltonian of the nanowire

$$
\begin{aligned}
H &= \int dy\, \Psi^\dagger(y)\, \mathcal{H} \Psi(y), && (4.1)\\
\mathcal{H}_\mathrm{nw} &= \frac{1}{2m^\star} \left(-i\hbar\nabla + e\mathbf{A}(y)\right)^2 \tau_z - i\hbar\alpha\partial_y\sigma_z\tau_z + \mathbf{B}\cdot\boldsymbol{\sigma} - \mu(y)\,\tau_z, && (4.2)\\
\Psi^\dagger(y) &= \left(\psi_\uparrow^\dagger(y), \psi_\downarrow^\dagger(y), \psi_\downarrow(y), -\psi_\uparrow(y)\right), && (4.3)
\end{aligned}
$$

where $\Psi^\dagger(y)$ contains electron creation and annihilation operators in the wire, $m^\star$ is the effective electron mass, α describes the spin-orbit coupling, $\mathbf{B}$ is the Zeeman field, and $\mu(y)$ is the chemical potential.

The Hamiltonian $H_\mathrm{T,N}$ describes the coupling of the nanowire to the normal lead. In the tight binding model $H_\mathrm{T,N}$ will connect modes in the normal lead to two points in the nanowire n_1, n_2

$$
H_\mathrm{T,N} = \sum_k t_\mathrm{N} c_{n_1 s}^\dagger a_{ks} + t_\mathrm{N} c_{n_2 s}^\dagger a_{ks} + \mathrm{h.c.}, \tag{4.4}
$$

with a_{ks} describing the lead modes with momentum k and spin s, and $c_{n_1 s}^\dagger$, $c_{n_2 s}^\dagger$ the creation operators for sites n_1, n_2 in the wire.

The Hamiltonian $H_\mathrm{T,SC}$ describes the coupling of the SC lead to the nanowire. To model the coupling to the SC correctly, we use the method described in Subsection 2.4.3. When describing the system using a tight binding model, this method prescribes coupling each point on the nanowire between y_b and y_e to an infinite superconductor,

Parameter	Symbol	Value
Wire Length	L	2500 nm
# Sites	N	90
TB Lattice parameter	a	27.7 nm
TB Hopping Term	t	2590 μeV
TB SO Term	u	360 μeV
SC Lead Length	L_{S}	1385 nm
SC Lead - Begin	y_{b}	554 nm
SC Lead - End	y_{e}	1939 nm
Effective Mass	$m^{\star}$	$0.019m_e$
SO Energy	E_{so}	50 μeV
SO Length	l_{so}	200 nm
Induced SC Gap	Δ_0	250 μeV
Chemical Potential	μ	125 μeV
Wire-SC coupling	$\pi\nu_0 t_{\mathrm{SC}}^2$	250 μeV
Wire-N coupling	$\pi\nu_0 t_{\mathrm{N}}^2$	98 μeV
N Lead Coupling Site	n_1	1
N Lead Coupling Site	n_2	10

Table 4.1: Tight binding parameters used in the simulation. The parameters correspond to a recent experiment [8]. The configuration is intended to be realistic and exhibits appreciable overlap between MBS.

producing a self energy term as described in Eq. 2.76.

The AB ring is formed in part by the normal lead, and by a section of the nanowire. To include the effect of the AB flux Φ, we choose the gauge described in Subsection 2.4.2. When writing the tight binding model of the system we will modify one of the hopping terms between two sites on the nanowire that are part of the ring, as described in Eq. 2.75. This allows us to modify only the Hamiltonian of the nanowire at one point, leaving the normal lead Hamiltonian and the Hamiltonian of the rest of the wire unaffected by the flux.

Using the above ingredients, we follow Section 2.4 and build a tight binding representation of the wire and leads. This representation allows us to calculate the conductance, visibility and local tunneling density of states of the system with different parameters supporting ABS, MBS or crossover states between them.

We will now present the configuration of the experimental setup. The parameters of the systems are taken to correspond to a recent experiment [8] (Table 4.1). The configuration parameters are taken to mimic a realistic system which exhibits an

appreciable overlap between the MBS.

Using the tight binding simulation we will show that the system exhibits zero bias peaks. At finite temperature, the system exhibits zero-energy ABS, zero-energy MBS, and zero-energy crossover MBS depending on the value of **B**. For every zero-energy state we will calculate the visibility of the conductance defined by changing the AB flux Φ.

Following the analytical results of Chapter 3, the visibility will be plotted as a function of temperature. For each state we will asses if the visibility can help us exclude the existence of well separated MBS. We will demonstrate that in some cases this measure is very useful in classifying the different states even at relatively high temperatures.

4.2 Wire Configuration

Using the parameters that appear in Table 4.1 we simulate the wire configuration. In Fig. 4.2a we present the differential conductance $^{d\langle\hat{I}\rangle}/_{V}$ in units of e^2/h as a function of the bias voltage V and Zeeman energy B, for temperature $T = 30\,\mathrm{mK}$. We apply the magnetic field **B** at an angle of 60° from the z axis in the yz plane. The dashed white line signifies the critical Zeeman energy for this system at $B_\mathrm{c} = \sqrt{\mu^2 + \Delta_0^2} = 279\,\mu\mathrm{eV}$ (Eq. 2.21) above which the system is in the topological phase in the thermodynamic limit (infinite wire length, L).

The ZBCPs we will focus on are listed in Table 4.2. Below the critical field B_c, where the system is in the topologically trivial phase, we observe a ZBCP ABS at $B_\mathrm{ABS} = 93.5\,\mu\mathrm{eV}$. Above B_c we observe a MBS at $B_\mathrm{MBS} = 365\,\mu\mathrm{eV}$ with splitting energy $E_\mathrm{M} = 0.006\,\mu\mathrm{eV}$. At higher magnetic fields we observe an oscillation in the

Type	$B\,[\mu eV]$	$E_\mathrm{M}\,[\mu eV]$
ABS	93.5	–
MBS	365	0.006
Crossover MBS	546	0.18
Crossover MBS	643	0.23

Table 4.2: Zero bias conductance peaks which we present. Detailed are the type of peak, Zeeman energy, and for the MBS at finite width we add energy splitting E_M.

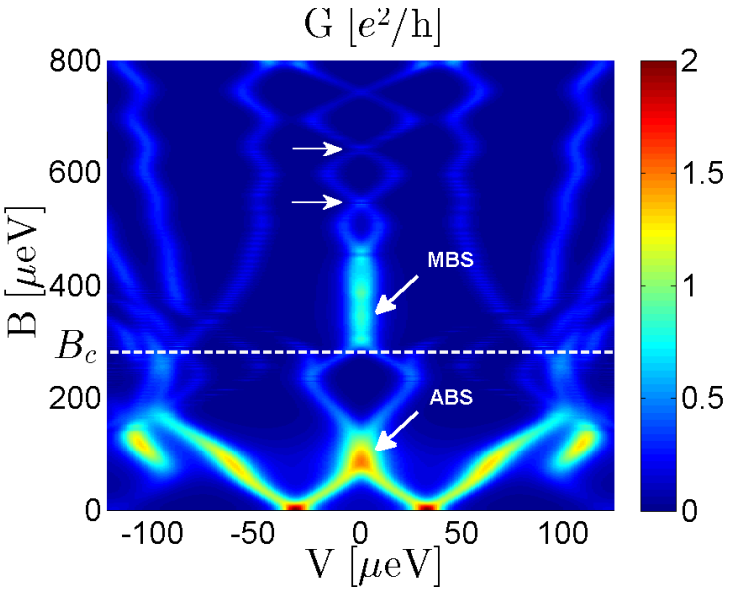

(a) Conductance overview $T = 30\,\mathrm{mK}$

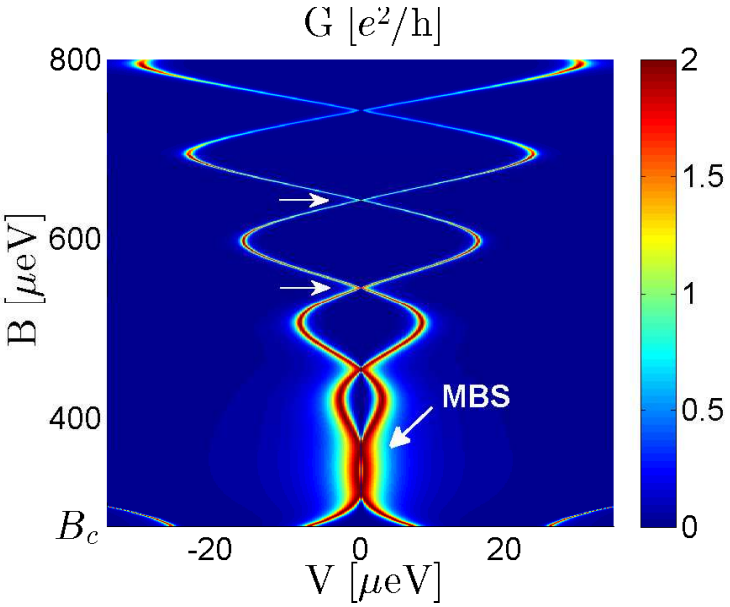

(b) Conductance MBS region $T = 0\,\mathrm{mK}$

Figure 4.2: Numerical simulation of the conductance as a function of bias V and Zeeman energy B for the configuration depicted in Fig. 4.1. The parameters correspond to a recent experiment [8], namely, we take the spin orbit energy to be $E_{\mathrm{so}} = 50\,\mu\mathrm{eV}$, the induced superconducting gap to be $\Delta_0 = 250\,\mu\mathrm{eV}$, and the spin orbit length to be $l_{\mathrm{so}} = 200\,\mathrm{nm}$. We take the length of the wire to be $L = 2.5\,\mu\mathrm{m}$ with $L_{\mathrm{S}} = 1385\,\mathrm{nm}$. The full set of parameters is listed in Table 4.1. We apply the magnetic field $\mathbf{B}$ at an angle of 60° from the z axis in the yz plane. (a) Wide overview of the conductance at temperature $T = 30\,\mathrm{mK}$ (b) Focus on the conductance of the MBS region $T = 0\,\mathrm{mK}$.

conductance due to the overlap between the two MBSs at the ends of the wire, we will refer to this as a crossover MBS. As a representative of the crossover MBSs we will focus on two states, one at $B_{\mathrm{cMBS}} = 546\,\mu\mathrm{eV}$ with splitting energy $E_{\mathrm{M}} = 0.18\,\mu\mathrm{eV}$ and another at $B_{\mathrm{cMBS}} = 643\,\mu\mathrm{eV}$ with splitting energy $E_{\mathrm{M}} = 0.23\,\mu\mathrm{eV}$.

We find the splitting E_{M} by setting a small t_{n} and measuring half the distance between the conductance peaks. For the MBS, each Zeeman energy B was chosen to locally minimize the splitting energy E_{M}. We differentiate between a MBS and crossover MBS by requiring the conductance to tend to $G = 2e^2/h$, and assuring that the size of the splitting energy is small compared to other energy scales in the problem (such as the coupling to the normal lead $\pi\nu_0 t_{\mathrm{N}}^2$).

To understand the splitting in the topological phase seen in Fig. 4.2b, we can model our system as two MBS with a finite energy splitting. The normal lead is assumed to be strongly coupled to one of the MBS and weakly coupled to the other. This model was considered in Subsection 2.1.3. Under these assumptions, at zero temperature, $T = 0$, the zero bias conductance should tend to zero $G(E = 0) \sim 0$, and at the splitting energy $E = \pm E_{\mathrm{M}}$ we expect a maximum of the conductance, which is close to $G(E = \pm E_{\mathrm{M}}) \sim 2e^2/h$. If we add a small temperature, we expect the peaks at $E = E_{\mathrm{M}}$ to smear, and in this case we should measure a finite zero bias conductance. This is a unique signature of the MBS which can be seen in Fig. 4.2.

In Fig. 4.3a,b we show the zero-energy differential conductance as a function of the Zeeman energy for $T = 0\,\mathrm{mK}$, $T = 30\,\mathrm{mK}$ respectively. In the third plot Fig. 4.3c we present the zero temperature conductance for $E = 0.94\,\mu\mathrm{eV}$. The plots depict two different conductance lines, the conductance at zero flux $G(\Phi = 0)$, and the maximal conductance when changing the flux between $\Phi = 0$ and $\Phi = \Phi_0$, we denote this $\max[G(\Phi)]$. Note that changing Φ does not change E_{M}, only the width of the conductance peaks Γ. The four black circles represent the four Zeeman energies we chose to focus on, i.e. the ABS, the MBS and two crossover MBS.

We observe that at zero temperature and zero bias (Fig. 4.3a) there is zero conductance above B_{c}, except for a single accidental non-topological subgap state at $B = 317\,\mu\mathrm{eV}$ which we choose to ignore. If we add finite temperature (Fig. 4.3b) or a small finite bias (Fig. 4.3c) we now observe a finite conductance.

Following Fig. 4.2b which shows the conductance at $T = 0$ in the MBS region ($B_{\mathrm{c}} < B < B_{\mathrm{max}}$), we see that the splitting of the MBS and the maximal conductance changes per Zeeman energy B. This data is presented in Fig. 4.3d. We see from this

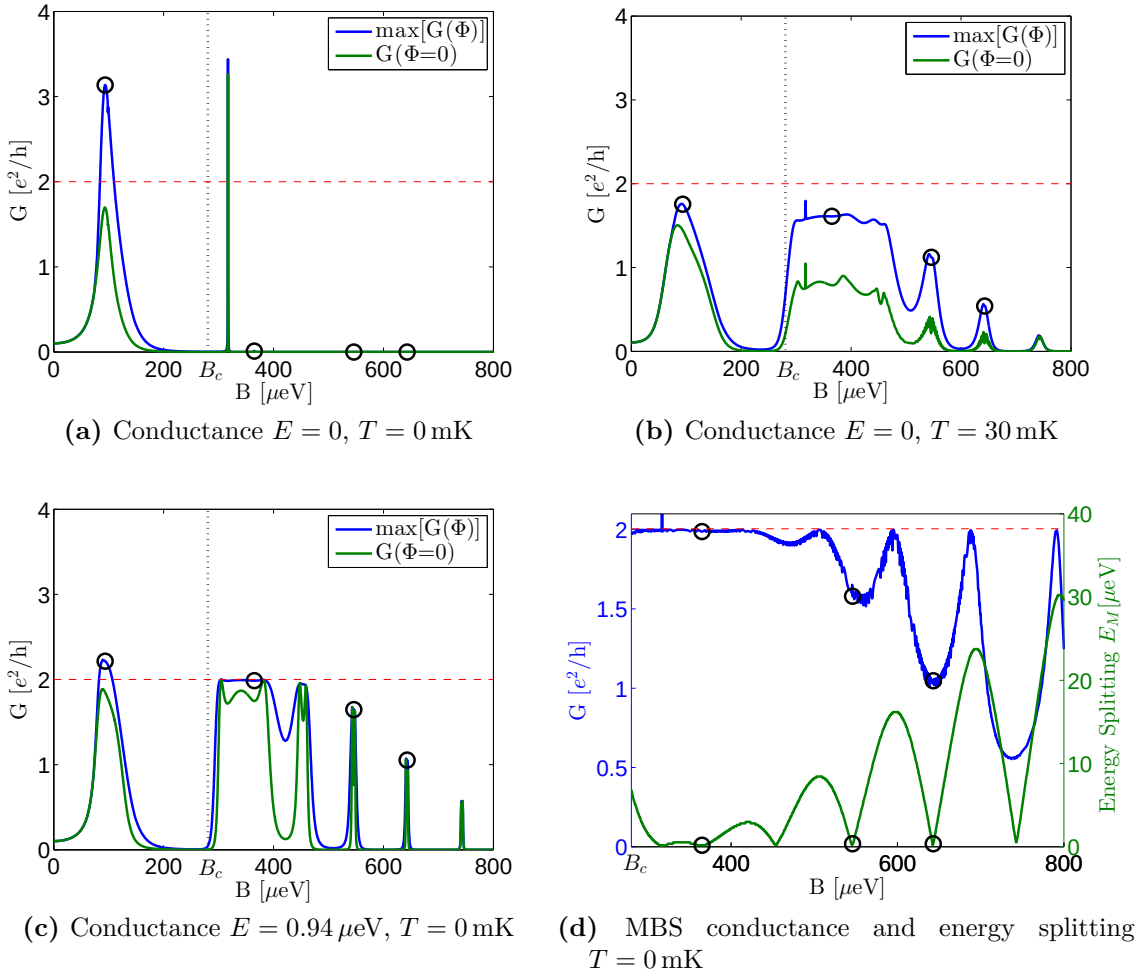

(a) Conductance $E = 0$, $T = 0\,\mathrm{mK}$

(b) Conductance $E = 0$, $T = 30\,\mathrm{mK}$

(c) Conductance $E = 0.94\,\mu\mathrm{eV}$, $T = 0\,\mathrm{mK}$

(d) MBS conductance and energy splitting $T = 0\,\mathrm{mK}$

Figure 4.3: Numerical simulation for the configuration depicted in Fig. 4.1. The parameters correspond to a recent experiment [8], namely $E_{\mathrm{so}} = 50\,\mu\mathrm{eV}$, $\Delta_0 = 250\,\mu\mathrm{eV}$, and $l_{\mathrm{so}} = 200\,\mathrm{nm}$. We take the length of the wire to be $L = 2.5\,\mu\mathrm{m}$ with $L_{\mathrm{S}} = 1385\,\mathrm{nm}$. The full set of parameters is listed in Table 4.1. We mark the four near zero states that we are interested in at Zeeman energies $B_{\mathrm{ABS}} = 93.5\,[\mu\mathrm{eV}]$, $B_{\mathrm{MBS}} = 365\,[\mu\mathrm{eV}]$, $B_{\mathrm{cMBS}} = 546\,[\mu\mathrm{eV}]$, $B_{\mathrm{cMBS}} = 643\,[\mu\mathrm{eV}]$ with black circles. (a)(b) Zero bias conductance as a function of Zeeman energy B for $T = 0\,\mathrm{mK}$, $T = 30\,\mathrm{mK}$ respectively. These correspond to Fig. 4.2a,b. The green line shows the conductance at $\Phi = 0$, while the blue line shows the maximal conductance over a flux quanta $\max\,[G(\Phi)]$. (c) Conductance as a function of Zeeman energy B for $E = 0.94\,\mu\mathrm{eV}$ and $T = 0$. This corresponds to Fig. 4.2b. (d) Maximal conductance of the MBS and energy splitting E_{M} as a function of Zeeman energy B at $T = 0\,\mathrm{mK}$. This corresponds to Fig. 4.2b. The splittings for both the MBS and the crossover MBS are relatively small, but the conductance for the MBS is close to $2e^2/h$, while for the crossover MBS it is appreciably less than $2e^2/h$.

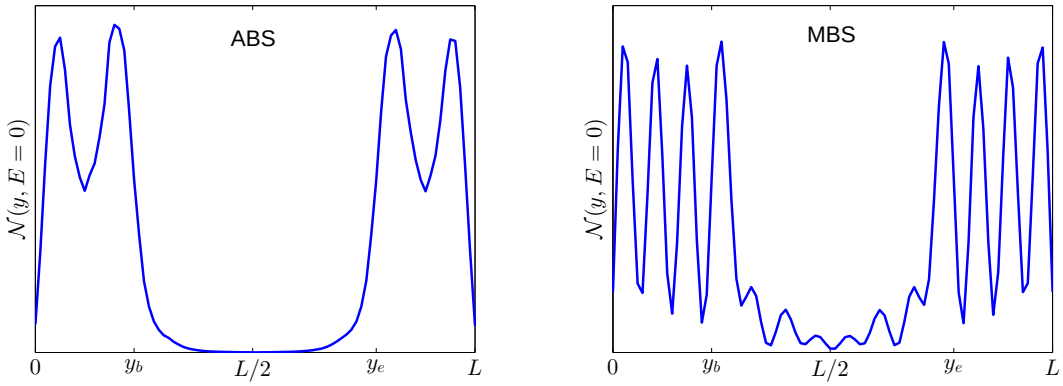

(a) Local tunneling density of state $E = 0$, $B_{\mathrm{ABS}} = 93.5\,\mu\mathrm{eV}$

(b) Local tunneling density of state $E = 0$, $B_{\mathrm{MBS}} = 365\,\mu\mathrm{eV}$

Figure 4.4: Local tunneling density of state at zero energy for the ABS at $B_{\mathrm{ABS}} = 93.5\,\mu\mathrm{eV}$ and the MBS at $B_{\mathrm{MBS}} = 365\,[\mu\mathrm{eV}]$. In both cases the density of states is significant only near the ends of the wire. The ABS decays exponentially inside the SC section, while the MBS decays exponentially with an oscillating component. For the MBS we see that the two MBS wavefunctions slightly overlap each other, causing a small energy splitting.

figure that $B_{\mathrm{MBS}} = 365\,\mu\mathrm{eV}$ is the only Zeeman energy for which the conductance is close to $G = 2e^2/h$ and the energy splitting E_{M} is small. The Zeeman energy $B = 317\,\mu\mathrm{eV}$ was excluded because it hosts a non-topological subgap state which has a conductance larger than $2e^2/h$. Other Zeeman energies have small energy splitting, but the conductance is appreciably smaller than $2e^2/h$, hence we call these states crossover MBS.

In Fig. 4.4a,b we present the local tunneling density of states at zero-energy $\mathcal{N}(y, E = 0)$ for the ABS and MBS respectively. We note that in both cases the LDOS is peaked in the normal sections of the wire. The ABS decays exponentially inside the SC section, while the MBS decays exponentially with an oscillating component. For the MBS we see that the two MBS wavefunctions slightly overlap each other, this causes a small energy splitting E_{M}. Both LDOS profiles are qualitatively similar to each other, making it difficult to distinguish between the ABS and the MBS using a scanning tunneling microscope measurement.

We now show that the visibility as a function of temperature (Fig. 4.5) can differentiate between the MBS and the ABS even at finite temperatures. We will specifically examine if it is possible to establish the trend of the visibility function

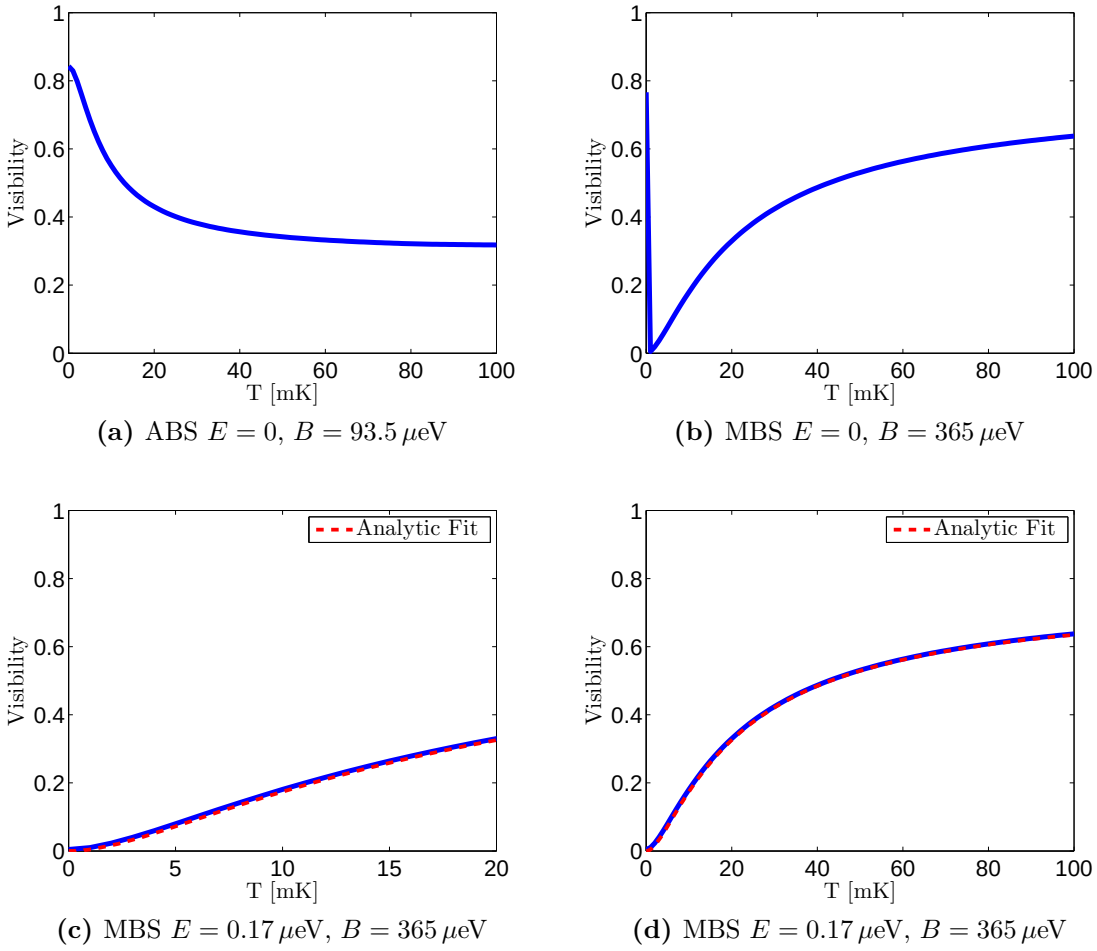

(a) ABS $E = 0$, $B = 93.5\,\mu$eV

(b) MBS $E = 0$, $B = 365\,\mu$eV

(c) MBS $E = 0.17\,\mu$eV, $B = 365\,\mu$eV

(d) MBS $E = 0.17\,\mu$eV, $B = 365\,\mu$eV

Figure 4.5: Visibility as a function of temperature. (a) Visibility for the ABS at $B_{\mathrm{ABS}} = 93.5\,\mu$eV. Monotonically decreasing function of temperature. This allows us to rule out the case of a MBS. (b) Visibility for the MBS at $B_{\mathrm{MBS}} = 365\,\mu$eV for $E = 0$. At high temperatures this is a monotonically increasing function of temperature. At low temperatures the dip in the conductance curve becomes apparent and the function decreases. If we want to measure a behavior consistent with the theory, we must measure the visibility close to the peak of the conductance which is at the splitting energy E_{M}. (c)(d) Visibility for the MBS at $B_{\mathrm{MBS}} = 365\,\mu$eV for $E = 0.17\,\mu$eV with an analytic fit. We fit the MBS visibility using the analytic expression for the visibility of an ideal MBS (Eq. 3.49) using two parameters Γ_{max}, Γ_{min} taken from Fig. 4.6. The measured visibility closely resembles the ideal MBS with a monotonically increasing function of temperature which tends to zero at zero temperature, and there is a qualitative agreement between the two.

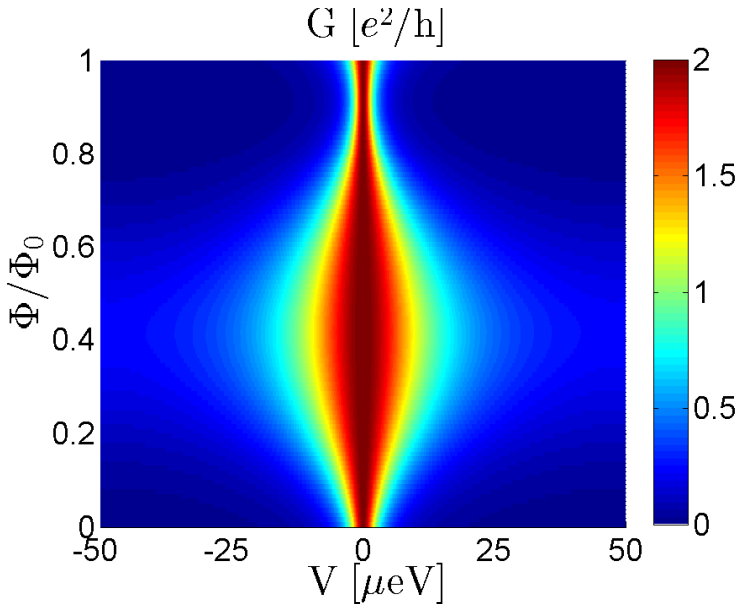

Figure 4.6: Zero temperature conductance as a function of bias V and AB flux $\frac{\Phi}{\Phi_0}$ for the MBS at $B_{\mathrm{MBS}} = 365\,\mu\mathrm{eV}$. This allows us to examine the width of the MBS peak with Φ. We measure the maximal and minimal width to be $\Gamma_{\max} = 12.27\,[\mu\mathrm{eV}]$, $\Gamma_{\min} = 1.64\,[\mu\mathrm{eV}]$.

by only sampling experimentally realizable temperatures between 20 mK and 50 mK. We present the plots for the ABS at $B_{\mathrm{ABS}} = 93.5\,[\mu\mathrm{eV}]$ in Fig. 4.5a. The MBS at $B_{\mathrm{MBS}} = 365\,[\mu\mathrm{eV}]$ is presented with zero bias in Fig. 4.5b, and with a small bias in Fig. 4.5c,d. The crossover MBS at $B_{\mathrm{cMBS}} = 546\,\mu\mathrm{eV}$, $B_{\mathrm{cMBS}} = 643\,\mu\mathrm{eV}$ are presented with zero bias in Fig. 4.7a,c and with a small bias in Fig. 4.7b,d.

In the case of the MBS at zero bias (Fig. 4.5b) the visibility is non-monotonic. At high temperatures the system resembles the topological MBS state, with the visibility being a monotonically increasing function of temperature. At low temperatures however, the non topological dip in the conductance curve is apparent, and the the function decreases. This is an immutable property of a finite system. A finite system will always have a finite energy splitting E_{M}, which causes a dip in conductance at zero bias. But the temperature at which the splitting is resolved decreases exponentially with the size of the system.

In the case of the MBS with a small finite bias (Fig. 4.5c,d) the visibility tends to zero at zero temperature and is a strictly increasing function of temperature. We see that when we look far from the dip in the conductance, the topological nature of the system persists even at small temperatures. The data agrees with the results of

Subsection 3.3.2. In the experimentally realizable temperatures region, we see that it is possible to establish a monotonically increasing trend for the visibility.

Using Eq. 3.49 we fit the MBS visibility using two parameters $\Gamma_{\max}$, $\Gamma_{\min}$. These parameters were taken from the zero temperature conductance of the MBS as a function of Φ (Fig. 4.6). The widths were found to be $\Gamma_{\max} = 12.27\,[\mu\text{eV}]$, $\Gamma_{\min} = 1.64\,[\mu\text{eV}]$. When we use the analytic expression to plot graphs of the visibility we find that they are qualitatively similar to the graphs of the numerical simulations. A comparison between the analytic expression and the numerical results is shown in Fig. 4.5c,d.

In the case of the ABS we have a monotonically decreasing visibility function (Fig. 4.5a). In the experimentally realizable temperatures region it possible to establish a monotonically decreasing trend, this allows us to rule out the existence of a MBS.

The crossover MBS however behaves qualitatively similar to the MBS (Fig. 4.7). For zero bias we have a non-monotonic visibility function (Fig. 4.7a,c). Specifically in this case we see that in the realizable temperatures region the visibility is monotonically increasing similar to the MBS. For a finite bias (Fig. 4.7b,d), the visibility is a strictly increasing function, but at zero temperature the function tends to a finite value instead of zero. However, this tendency is probably impossible to measure in a real experiment.

4.3 Conclusion

In conclusion we saw that the visibility of a MBS state increases with temperature. For a finite wire with small splitting energy the behavior is more complex and we have analyzed and understood the behavior in different situations. We note that the success of this method highly depends on the details of the problem, as explained in the conclusions to the analytic calculations (Section 3.4). It can only be used to rule out well separated MBS, and in no way can it confirm it. In our simulation we were only able to rule out the ABS, with the crossover MBS behaving qualitatively similar to the MBS.

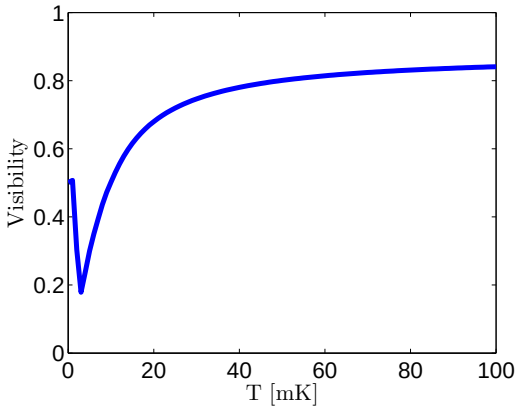

(a) Crossover MBS $E = 0$, $B = 546\,\mu$eV

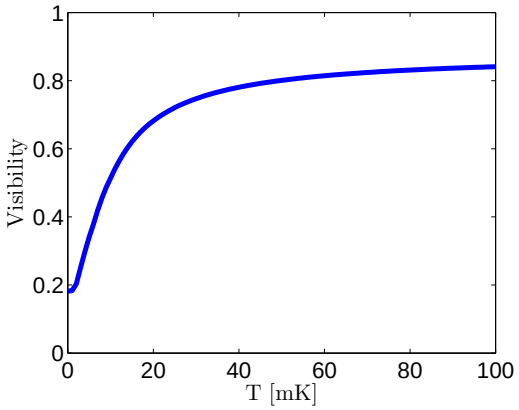

(b) Crossover MBS $E = 0.35\,\mu$eV, $B = 546\,\mu$eV

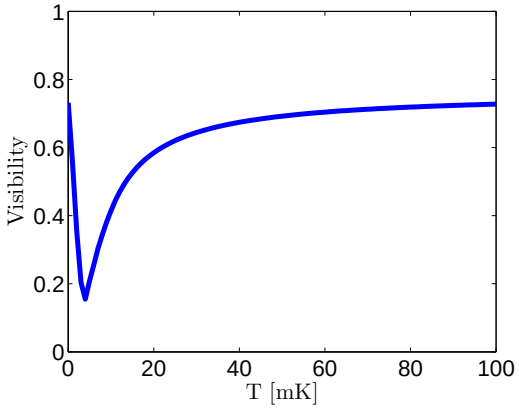

(c) Crossover MBS $E = 0$, $B = 643\,\mu$eV

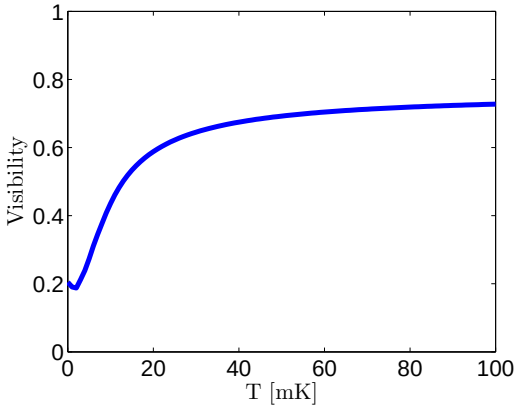

(d) Crossover MBS $E = 0.45\,\mu$eV, $B = 546\,\mu$eV

Figure 4.7: Visibility as a function of temperature for the crossover MBSs. (a)(c) For $E = 0$, we see that at high temperatures they are monotonically increasing functions of temperature. At low temperatures the dip in the conductance curve becomes apparent and the functions decrease. (b)(d) For finite bias, the functions are monotonically increasing with temperature, but they do not tend to zero at zero temperature as expected of an ideal MBS. This is in contrast to the behavior of the visibility of the MBS at $B = 365\,\mu$eV which is shown in Fig. 4.5c,d.

5 Discussion

In recent years the semiconducting Majorana wire has attracted considerable attention as a result of the recently reported experimental evidence for both the ZBCP and the fractional AC Josephson effect in the form of doubled Shapiro steps. Although the experimentally observed signatures can be taken as necessary indications of a Majorana bound state, there still exist alternative explanations to these observations. The fractional Josephson effect in semiconductor Majorana wires is susceptible to the quasiparticle poisoning effect, as well as to non-adiabaticity effects. While for the ZBCP, other sources of low-energy states localized at the wire boundary may produce similar zero-bias peaks. Thus, neither of them constitutes a sufficient "smoking gun" experiment.

Finding a single measurement which is immune to any sort of imitation is an extremely difficult task. It is clear that the definitive confirmation of the MBS will be a direct probe of its non-Abelian nature. Such a measurement is a complicated technological feat, and it is unclear how much time will pass until experimentalists achieve this goal. Until this ultimate confirmation will occur, it is important to strengthen the case of the Majorana by observing as many different experimental signatures as possible. With this idea in mind, we started the research for this Thesis. Our aim was to find an experimental signature of the MBS that is simple to measure in the lab.

We proposed using a normal lead with an Aharonov-Bohm flux ring as a probe, and connecting this lead to the Majorana bound state. In such a setup, we suggested measuring the visibility of the zero bias conductance peak as a function of temperature. Usually decoherence effects increase with temperature, hence we expect that the visibility will decrease with the temperature. In striking contrast, we find that for Majorana bound states with zero splitting energy $E_{\mathrm{M}} = 0$, the visibility is a strictly increasing function of temperature, with zero visibility at zero temperature. While for a low energy Andreev bound state we showed that the visibility can

assume increasing, decreasing, constant or non-monotonic behavior.

In the numerical simulation of the Majorana wire we saw that the MBSs exhibit energy splitting $E_{\mathrm{M}} > 0$, which is caused by the finite nature of the wire. The zero bias conductance for such a state is close to zero, while the conductance at the splitting energy is close to $2e^2/h$ in our model (generally it is less than $2e^2/h$). For modes in which the splitting is small and the conductance is close to $2e^2/h$ we still use the name MBSs. While for modes in which the conductance is appreciably less than $2e^2/h$, or the splitting is large, we use the name crossover MBSs. In the simulation we saw the Majorana zero bias peak appear at the predicted critical field. For larger magnetic fields the MBSs split into two modes and become crossover MBSs.

We further saw that the zero bias visibility of a MBS acts as expected for large temperatures. But for small enough temperatures the splitting becomes apparent and the visibility decreases as a function of temperature. In this case, if we want to measure a behavior consistent with the theory, we must measure the visibility at the peak of the conductance which is at the splitting energy E_{M}. For the Andreev state the visibility was a decreasing function of temperature. This allowed us to rule out the case of a Majorana bound state. In principle, the Andreev state could have also been an increasing function of temperature, in which case we could not have used our criteria. However, in contrast to the robustness of the Majorana state, we expect that the behavior of the visibility of the Andreev state will be more sensitive to changes in the parameters of the system.

As for future research directions, it would be interesting to extend the work in several way. First, we only considered a low energy ABS as an alternative theory to the MBS. In order to increase the predictive power of the method, it would be imperative to calculate the visibility as a function of temperature of more alternative explanations such as the Kondo effect and weak anti-localization. If the visibilities of other theories also behave in the same way as a MBS, this would detract from the usefulness of the method. Second, in this Thesis we only considered setups which include grounded superconductors when constructing the Majorana states. This corresponds to a non-interacting picture leading to the resonant Andreev reflection scenario. If we consider a floating superconductor, then Coulomb interactions become important and they profoundly change this picture. It would be interesting to see if the visibility behaves differently with the inclusion of Coulomb interactions.

Bibliography

[1] Jason Alicea. New directions in the pursuit of Majorana fermions in solid state systems. *Rep. Prog. Phys.*, 75(7):076501, July 2012.

[2] Jay D. Sau, Roman M. Lutchyn, Sumanta Tewari, and S. Das Sarma. Generic New Platform for Topological Quantum Computation Using Semiconductor Heterostructures. *Phys. Rev. Lett.*, 104(4):040502, January 2010.

[3] Jay D. Sau, Sumanta Tewari, Roman M. Lutchyn, Tudor D. Stanescu, and S. Das Sarma. Non-Abelian quantum order in spin-orbit-coupled semiconductors: Search for topological Majorana particles in solid-state systems. *Phys. Rev. B*, 82(21):214509, December 2010.

[4] Roman M. Lutchyn, Jay D. Sau, and S. Das Sarma. Majorana Fermions and a Topological Phase Transition in Semiconductor-Superconductor Heterostructures. *Physical Review Letters*, 105:077001, August 2010.

[5] Yuval Oreg, Gil Refael, and Felix von Oppen. Helical Liquids and Majorana Bound States in Quantum Wires. *Phys. Rev. Lett.*, 105(17):177002, October 2010.

[6] Johan Nilsson, A. R. Akhmerov, and C. W. J. Beenakker. Splitting of a Cooper pair by a pair of Majorana bound states. *Physical Review Letters*, 101(12), September 2008.

[7] K. T. Law, Patrick A. Lee, and T. K. Ng. Majorana Fermion Induced Resonant Andreev Reflection. *Physical Review Letters*, 103(23), December 2009.

[8] V. Mourik, K. Zuo, S. M. Frolov, S. R. Plissard, E. P. a. M. Bakkers, and L. P. Kouwenhoven. Signatures of Majorana Fermions in Hybrid Superconductor-Semiconductor Nanowire Devices. *Science*, 336(6084):1003–1007, May 2012.

[9] M. T. Deng, C. L. Yu, G. Y. Huang, M. Larsson, P. Caroff, and H. Q. Xu. Anomalous Zero-Bias Conductance Peak in a Nb–InSb Nanowire–Nb Hybrid Device. *Nano Lett.*, 12(12):6414–6419, December 2012.

[10] Anindya Das, Yuval Ronen, Yonatan Most, Yuval Oreg, Moty Heiblum, and Hadas Shtrikman. Zero-bias peaks and splitting in an Al-InAs nanowire topological superconductor as a signature of Majorana fermions. *Nat Phys*, 8(12):887–895, December 2012.

[11] S. Sasaki, S. De Franceschi, J. M. Elzerman, W. G. van der Wiel, M. Eto, S. Tarucha, and L. P. Kouwenhoven. Kondo effect in an integer-spin quantum dot. *Nature*, 405(6788):764–767, June 2000.

[12] D. I. Pikulin, J. P. Dahlhaus, M. Wimmer, H. Schomerus, and C. W. J. Beenakker. A zero-voltage conductance peak from weak antilocalization in a Majorana nanowire. *New J. Phys.*, 14(12):125011, December 2012.

[13] A. Yu Kitaev. Unpaired Majorana fermions in quantum wires. *Phys.-Usp.*, 44(10S):131, October 2001.

[14] Jason Alicea, Yuval Oreg, Gil Refael, Felix von Oppen, and Matthew P. A. Fisher. Non-Abelian statistics and topological quantum information processing in 1d wire networks. *Nature Physics*, 7(5):412–417, May 2011.

[15] Supriyo Datta. *Electronic Transport in Mesoscopic Systems*. Cambridge University Press, May 1997.

[16] B. Andrei Bernevig and Taylor L. Hughes. *Topological Insulators and Topological Superconductors*. Princeton University Press, 2013.

[17] Jie Liu, Andrew C. Potter, K. T. Law, and Patrick A. Lee. Zero-Bias Peaks in the Tunneling Conductance of Spin-Orbit-Coupled Superconducting Wires with and without Majorana End-States. *Phys. Rev. Lett.*, 109(26):267002, December 2012.

[18] Yuval Oreg. Universal phase lapses in a noninteracting model. *New J. Phys.*, 9(5):122, May 2007.

[19] Arbel Haim, Erez Berg, Felix von Oppen, and Yuval Oreg. Signatures of Majorana Zero Modes in Spin-Resolved Current Correlations. *Phys. Rev. Lett.*, 114(16):166406, April 2015.

[20] G. E. Blonder, M. Tinkham, and T. M. Klapwijk. Transition from metallic to tunneling regimes in superconducting microconstrictions: Excess current, charge imbalance, and supercurrent conversion. *Phys. Rev. B*, 25(7):4515–4532, April 1982.

[21] Yositake Takane and Hiromichi Ebisawa. Conductance Formula for Mesoscopic Systems with a Superconducting Segment. *J. Phys. Soc. Jpn.*, 61(5):1685–1690, May 1992.

[22] H. O. H. Churchill, V. Fatemi, K. Grove-Rasmussen, M. T. Deng, P. Caroff, H. Q. Xu, and C. M. Marcus. Superconductor-nanowire devices from tunneling to the multichannel regime: Zero-bias oscillations and magnetoconductance crossover. *Phys. Rev. B*, 87(24):241401, June 2013.

[23] G. Kells, D. Meidan, and P. W. Brouwer. Near-zero-energy end states in topologically trivial spin-orbit coupled superconducting nanowires with a smooth confinement. *Phys. Rev. B*, 86(10):100503, September 2012.

[24] Dmitry Bagrets and Alexander Altland. Class D Spectral Peak in Majorana Quantum Wires. *Phys. Rev. Lett.*, 109(22):227005, November 2012.

[25] Eduardo J. H. Lee, Xiaocheng Jiang, Manuel Houzet, Ramón Aguado, Charles M. Lieber, and Silvano De Franceschi. Spin-resolved Andreev levels and parity crossings in hybrid superconductor-semiconductor nanostructures. *Nat Nano*, 9(1):79–84, January 2014.

Nomenclature

AB ring	Aharonov-Bohm ring
ABS	Andreev bound state
DOS	Density of states
LDOS	Local tunneling density of states
MBS	Majorana bound state
MF	Majorana fermion
ZBCP	Zero bias conductance peak